Crossing hydrological and geochemical modeling to understand the spatiotemporal variability of water chemistry in an elementary watershed (Strengbach, France)

Julien Ackerer, Benjamin Jeannot, Frederick Delay, Sylvain Weill, Yann Lucas, Bertrand Fritz, Daniel Viville, François Chabaux.

Laboratoire d'Hydrologie et de Géochimie de Strasbourg, Université de Strasbourg, CNRS, ENGEES, 1 rue Blessig, 67084 Strasbourg Cedex, France

Corresponding authors : Julien Ackerer, Benjamin Jeannot, Frederick Delay (fdelay@unistra.fr), François Chabaux (fchabaux@unistra.fr)

Abstract

Understanding the spatiotemporal variability of the chemical composition of surface waters is a major issue for the scientific community, especially given the prospect of significant environmental changes over the next decades. To date, the study of concentration-discharge relationships has been widely used to assess the spatiotemporal variability of the water chemistry over watersheds. However, the lack of independent estimations of water transit times within catchments limits our ability to model and predict the water chemistry by relying upon geochemical approaches only. This study shows the potential of coupling hydrological and hydrogeochemical modeling to better understand the spatiotemporal variability of the composition of surface waters. In a first step, a dimensionally reduced hydrological model coupling surface flow with subsurface flow (i.e., the Normally Integrated Hydrological Model, NIHM) has been used to constrain the distribution of the flow lines that are feeding the springs. In a second step, hydrogeochemical simulations with the code KIRMAT (KInectic Reaction and MAss Transport) have been performed to calculate the evolution of the water chemistry along the flow lines. The results indicate that the concentrations of dissolved silica (H_4SiO_4) and basic cations (Na^+, K^+, Mg^{2+}, and Ca^{2+}) in the spring waters are correctly reproduced with a simple integration along the flow lines. The water chemistry and clay mass fractions are also correctly captured when clays are handled as solid solutions. The weak variabilities over time in the spatial flow distribution and water velocities render mean transit time of waters that span the

41 narrow range of 1.5 to 3 months in the watershed. These findings indicate that the chemostatic
42 behavior of the spring chemistry is a direct consequence of the strong hydrological control
43 exerted on water transit times within the catchment. The good matching between the
44 measured and modeled concentrations while respecting durations of water-rock interactions
45 provided by hydrological simulations also shows that the chemical composition of waters can be
46 captured by relying upon simply determined reactive surfaces and experimental kinetic
47 constants. These results reinforce the idea that the low surfaces (< 1 m^2/g) calculated from the
48 geometrical shapes of primary minerals are valuable estimates of the reactive surfaces within
49 natural environments. The originality of this study is to cross hydrological and geochemical
50 modeling to understand the spatiotemporal variability of hydrogeochemical processes in a
51 mountainous catchment with highly transient hydrological behavior and short water transit
52 times in the subsurface.

1- Introduction

Understanding the effects of the ongoing climatic changes on the environment is a major issue for the coming years. The global increase of temperature is expected to affect the hydrological cycle at a large scale, and providing a precise estimation of its repercussion on the evolution of soils and on the chemistry of waters remains challenging. This challenge is associated with the diversity of hydrological, geochemical, biological processes, and their coupling, that operate over continental land surfaces (e.g., Gislason et al., 2009; Goddéris et al., 2013; Beaulieu et al., 2012; 2016). Up to now, the study of concentration-discharge relationships has been widely used to assess the coupling between hydrological and geochemical processes at the watershed scale (Kim et al., 2017; Ameli et al., 2017). However, these concentration-discharge relationships are mainly qualitative, and the lack of independent estimates of water transit times limits the ability to model and predict solute mass transfers within catchments. A precise knowledge of the water flow paths and their variability from wet to dry seasons is an important new step to constrain the water transit times within catchments, and then decipher the seasonal fluctuations of the composition of waters. Understanding the variability of water geochemical compositions will require further development of modeling approaches able to combine hydrological and geochemical processes (Kirchner, 2006).

Recent efforts in hydrological modeling were conducted to develop spatially distributed approaches that better consider the interplay between surface and subsurface processes (e.g., Gunduz and Aral, 2005; Kampf and Burges, 2007; Camporese et al., 2010). Due to the complexity of flows in the hydrological processes, several modeling approaches are based on the full resolution of the Richards and Saint-Venant equations to correctly describe the

interactions between stream, overland and subsurface waters (Kampf and Burges, 2007). These approaches have shown their ability to capture the hydrological functioning of various watersheds, knowing that the full resolution of the Richards and Saint-Venant equations is computationally demanding and faces calibration and parameterization difficulties (Ebel and Loague, 2006; Mirus et al., 2011). Questions have been raised regarding the optimal complexity of the equations that are needed to correctly treat the hydrology of catchments in their surface and subsurface compartments with reasonable computation times (Gunduz and Aral, 2005). Low-dimensional and depth-integrated models have attracted growing interest because they represent an interesting compromise between the system complexity, the calculation efforts, and the quality of results (Pan et al., 2015; Hazenberg et al., 2016; Weill et al., 2013; 2017; Jeannot et al., 2018). These depth-integrated models recently demonstrated their ability to reproduce the results from fully dimensioned approaches in small catchments while reducing computational costs (Pan et al., 2015; Jeannot et al., 2018). Nonetheless, the water transit times calculated from these depth-integrated models are rarely confronted with the water-rock interaction times inferred from hydrogeochemical modeling of water chemistry in watersheds.

For its part, the understanding of the hydrogeochemical functioning of the critical zone has been significantly improved by the implementation of reactive-transport processes in geochemical modeling tools (Steefel et al., 2005; Lucas et al., 2010; 2017; Goddéris et al., 2013; Li et al., 2017). These developments allow for considering a variety of processes, such as flow and transport, ion exchanges, biogeochemical reactions, and the interplay between primary mineral dissolution and secondary mineral precipitation (Moore et al., 2012; Lebedeva and Brantley, 2013; Ackerer et al., 2018). Reactive transport models have been used to explore a

97 wide variety of scientific issues, including the study of global atmospheric CO_2 consumption by
98 weathering reactions (Goddéris et al., 2013; Li et al., 2014), the formation and evolution of soil
99 and regolith profiles (Maher et al., 2009; Navarre-Sitchler et al., 2009; Lebedeva and Brantley,
100 2013), and the variability of water quality and chemistry in the environment (Lucas et al., 2010;
101 2017; Ackerer et al., 2018). However, these approaches usually refer to a simple one-
102 dimensional flow path through a regolith column or along a hill slope to model flow in the
103 system (e.g., Maher et al., 2011; Moore et al., 2012; Lucas et al., 2017; Ackerer et al., 2018). If
104 these approaches are useful to discuss the key processes involved in the regolith formation and
105 the acquisition of the water chemical composition, such one-dimensional transport reactive
106 modeling cannot take into account the diversity or the complexity of the flow trajectories in
107 watersheds; hence, its effects on the water chemistry at the watershed scale.

108 A new step is therefore necessary for the development of hydrogeochemical modeling
109 approaches that are applicable at the watershed scale and are able to integrate the complexity
110 of the water flows and the diversity of the water-rock interaction processes. Recent efforts have
111 been undertaken in this direction by merging hydrological and geochemical codes, as for
112 example the reactive transport code ParCrunchFlow (Beisman et al., 2015), or the coupled
113 hydrogeochemical code RT-Flux-PIHM (Li et al., 2017). An alternative to solving fully
114 dimensioned problems is given in the present study by considering an original dimensionally-
115 reduced approach, with modest computation times even when applied at the scale of a whole
116 watershed. The approach combines for the first time in this manner the results from a
117 hydrological depth-integrated and spatially distributed model (NIHM) with a reactive transport
118 model (KIRMAT). Such coupling allows for modeling the spatial and temporal distribution of the

flow trajectories and associated flow rates, the weathering reactions, and the evolution of the water chemistry within an elementary watershed. The Strengbach catchment targeted by this study is one of the reference observatories of the French critical zone network (OZCAR, http://www.ozcar-ri.org), where multidisciplinary studies, including hydrological, geochemical and geological investigations, have been performed since 1986 ("Observatoire Hydrogéochimique de l'Environnement", OHGE; http://ohge.unistra.fr ; El Gh'Mari, 1995; Fichter et al., 1998; Viville et al., 2012; Gangloff et al., 2014; 2016; Pierret et al., 2014; Prunier et al., 2015; Pan et al., 2015; Ackerer et al., 2016; 2018; Beaulieu et al., 2016; Chabaux et al., 2017; Schmitt et al., 2017; 2018; Daval et al., 2018). The method proposed in this work will yield precise knowledge of the water flow paths and their variability from wet to dry seasons, which is an important new step to better constrain the water transit times within catchments and to correctly understand the seasonal fluctuations in water chemistry.

2- Site presentation and data acquisition

The Strengbach catchment is a small watershed (0.8 km^2) located in the Vosges Mountains of northeastern France at altitudes between 883 and 1147 masl. Its hydroclimatic characteristics can be found in Viville et al. (2012) or in Pierret et al. (2014). It is marked by a mountainous oceanic climate, with an annual mean temperature of 6 $^{\circ}C$ and an annual mean rainfall of approximately 1400 mm, with 15 to 20% falling as snow during two to four months per year. The snow cover period is quite variable from year to year, and may not be continuous over the entire winter. The annual mean evapotranspiration is of approximately 600 mm, and the annual mean runoff of approximately 800 mm (in Viville et al., 2012). The watershed is currently covered by a beech and spruce forest. The bedrock is a base-poor Hercynian granite covered by

141 a 50 to 100 cm-thick acidic and coarse-in-texture soil. The granitic bedrock was fractured and
142 hydrothermally altered, with a stronger degree of hydrothermal overprinting in the northern
143 than the southern part of the catchment (Fichter et al., 1998). The granite was also affected by
144 surface weathering processes during the Quaternary (Ackerer et al., 2016). The porous and
145 uppermost part of the granitic basement constitutes an aquifer from 2 to approximately 10
146 meters thickness. In the Strengbach watershed, the major floods and high-flow events usually
147 occur during snowmelt periods at the end of the winter season or in the early spring. In
148 contrast, the low-flow periods commonly happen at the end of the summer or during the
149 autumn. Several springs naturally emerge along the slopes (figure 1). The watershed has been
150 equipped with several piezometers and boreholes since 2012, those being located along the
151 slopes on both sides of the watershed (figure 1; Chabaux et al., 2017). Spring waters are
152 regularly collected and analyzed since 2005, with monthly sampling campaigns completed by
153 occasional specific samplings to cover the entire range of water discharges in the system.
154 Piezometer waters have only been collected during specific sampling campaigns over the period
155 2012-2015, and as for the spring waters, these samplings cover different hydrological conditions
156 from wet to dry periods. The soil solutions are collected with a monthly frequency on the
157 southern slope at a beech plot (named HP) and to the north at a spruce plot (named VP; figure
158 1; more details are provided in Prunier et al., 2015). For all the collected waters, the
159 concentrations of the major dissolved species and the pH were determined by following the
160 analytical techniques used at LHyGeS (Strasbourg, France) and detailed in Gangloff et al. (2014)
161 and Prunier et al. (2015). Discharges of water from the springs were measured during the
162 sampling campaigns, as were the water levels within the piezometers. The mineralogy and the

163 porosity of the bedrock have been studied in detail in previous studies (El Gh'Mari, 1995; Fichter
164 et al., 1998). On the southern part of the catchment, the weakly hydrothermally altered granite
165 (named HPT, figure 1) is mainly composed of quartz (35%), albite (31%), K-feldspar (22%) and
166 biotite (6%). It also contains small amounts of muscovite (3%), anorthite (2%), apatite (0.5%)
167 and clay minerals (0.5%). On the northern part of the catchment, the lithology is more variable,
168 with the presence of gneiss close to the crest lines and the occurrence of hydrothermally
169 altered granite on the rest of the slopes (El Gh'Mari, 1995, figure 1). The hydrological,
170 geochemical and petrological data obtained from these field investigations are the basis of the
171 modeling work presented in this study. More precisely, this study is based on hydrogeochemical
172 data from 2005 to 2015 for waters from four springs of the southern part (CS1, CS2, CS3 and
173 CS4) and one spring of the northern part (RH3) of the watershed. Hydrogeochemical data
174 obtained over the period 2012-2015 for two piezometers (PZ3, PZ5) of the southern part of the
175 watershed are also studied. The complete hydrogeochemical database is available as
176 supplementary material appended to this work (tables EA1 to EA9). The specific chemical data
177 from spring and piezometer waters modeled in this study are reported in table 1.

178 **3- Modeling methods**

179 The modeling developments presented herein are a new step in the efforts undertaken at
180 LHyGeS to constrain the mechanisms controlling the geochemical composition of surface waters
181 and to understand their spatial and temporal variability at the scale of elementary mountainous
182 watersheds (Schaffhauser et al., 2014; Lucas et al., 2017; Ackerer et al., 2018). The main
183 innovation of this work is to couple a spatially distributed hydrological model with a reactive
184 transport model to constrain the spatiotemporal variability of chemical composition of spring

and piezometer waters from the Strengbach watershed. To the best of our knowledge, this is the first time that such a coupling between hydrological and hydrogeochemical modeling approaches has been attempted at the watershed scale. The hydrological model determines the distribution of the water flow lines within the watershed and thus constrains the water transit times for any period (summer or fall droughts, winter or spring floods). Then, the hydrogeochemical model is used to simulate the acquisition and the evolution of the water chemistry along the determined flow lines within the catchment.

3-1 Hydrological modeling

To assess the water flows in the watershed, several simulations were performed with the hydrological code NIHM (Normally Integrated Hydrological Model; Pan et al., 2015; Weill et al., 2017; Jeannot et al., 2018). This code is a coupled stream, overland, and depth-integrated subsurface flow model developed at LHyGeS and already tested in the Strengbach watershed (Pan et al., 2015). The stream and overland flows are described by a diffusive-wave equation, and the subsurface flow is handled through an integration (in a direction normal to bedrock) of the unsaturated-saturated flow equation from the bedrock to the soil surface (Weill et al., 2017). Water exchange between the surface and the subsurface compartments are addressed via the hydraulic head differences between the compartments (Jeannot et al., 2018).

Regarding the hydrological simulations, the parameters of the aquifer were adjusted in NIHM through a calibration-validation procedure. Several zones of heterogeneity were defined based on field observations (Ackerer et al., 2016; Chabaux et al., 2017). In each zone, the saturated hydraulic conductivity, the depth of the substratum, and the porosity, were set to uniform

206 values, but varying from one zone to the other. Other parameters were set to uniform values
207 over the whole catchment (see table 2). The aquifer thickness that was used for the simulations
208 varied from 2 m near the main crests to up to 8 m in the middle of the watershed (figure 2), in
209 agreement with data collected during the recent geological investigations and drilling
210 campaigns undertaken at the catchment (Ackerer et al., 2016; Chabaux et al., 2017). The
211 uniform precipitations over space applied at the surface of the catchment are drawn from data
212 of the rain gauge station located at the highest elevation of the watershed (site PA, figure 1).
213 The hydrological model NIHM was then run on a first time period (year 1996-1997). The model
214 parameters (table 2) were gradually modified within a simple trial and error process to improve
215 the fit between observed and simulated flow rates of the stream at the outlet of the catchment
216 (these flow rates are the only reliable hydrological data informing on surface and subsurface
217 flow at the catchment scale). The quality of fitting was evaluated via the root mean squared
218 error (RMSE) between observations and simulations, and the Kling-Gupta efficiency coefficient
219 (KGE; Gupta et al., 2009). Once the best fit was obtained, the model was then run over another
220 time period (2010-2015) without changing the parameters anymore, and the quality of the fit
221 was re-assessed on this new time period via the RMSE and KGE indicators. Figure 2 shows the
222 result for the 2010-2015 time period. Once the water discharges were correctly reproduced at
223 the outlet, a backtracking approach was used to constrain the origin of subsurface water exiting
224 the system at prescribed locations, and the spatiotemporal variability of the flow lines within
225 the watershed. To back track the water particles, the velocity fields calculated by the NIHM
226 model were inverted in their direction, and the locations of the backtracked particles were
227 saved at each time-step. A daily time-step was used for the backtracking, as a compromise

between computational efforts and a refined description of the transient velocity fields. A schematic representation of the backtracking approach is given in figure 3. This methodology allows for delineating the flow paths that bring water at a given time and a given location within the catchment. This information is of major interest to determine the origin of the spring and piezometer waters. It is shown at the catchment scale, that flow is mainly driven by gravity in association with the steep slopes of the watershed, the latter being almost evenly drained over its whole surface area (figure 4). For each water sampling area, ten flow lines that bring water to the location of interest were determined (figure 4), together with a few features of the flow lines, including: local velocities, mean velocities, and length of the flow paths. It is worth noting that times calculated along the streamlines correspond to a date, x days before arrival, at which a water particle entered the subsurface or passed at a given location along the streamline. Streamlines calculated via backtracking and reaching sampling sites only consider flow in the subsurface compartment (but there is no diffuse surface flow at the Strengbach catchment except routing via the stream network) and are conditional to an arrival date at a prescribed location. As streamlines are not associated with calculations of water flux values, the time distributions drawn from streamline calculations are only an approximation of the actual transit time distributions. An even weight is given to each calculated time, when an exact distribution should weight each time by the mass of water conveyed.

3-2 Hydrogeochemical modeling

The simulations of the water chemical composition along the flow lines were performed with the hydrogeochemical KIRMAT code (KInectic of Reaction and MAss Transport; Gérard et al., 1998; Lucas et al., 2010; Ngo et al., 2014). KIRMAT is a thermo-kinetic model based on the

Transition State Theory (TST, Eyring, 1935; Murphy and Helgeson, 1987) that simultaneously solves equations describing geochemical reactions and transport mass balance in a 1D-porous medium. The mass transport includes the effects of one-dimensional convection, diffusion and kinematic dispersion. Chemical reactions account for the dissolution of primary minerals and oxido-reduction reactions, in addition to the formation of secondary minerals and clay minerals. The clay fraction is defined as a solid solution made up of a combination of pure clay end-members. The clay end-members are defined on the basis of X-ray diffraction analyses of clay minerals present in bedrock samples collected in the field (Fichter et al., 1998; Ackerer et al., 2016; 2018). During the hydrogeochemical simulations, the clay solid solution is precipitated at thermodynamic equilibrium and its composition varies over time, depending on the evolution of the water chemistry and the bedrock mineralogy (Ackerer et al., 2018). This multicomponent solid solution reproduces the non-pure composition of clay phases resulting from low-temperature water-rock interactions (Tardy and Fritz, 1981). The KIRMAT code also accounts for the feedback effects between mineral mass budgets, reactive surfaces, and porosity evolution (Ngo et al., 2014). The reactive surfaces of the primary minerals were calculated by assuming a simple spherical geometry for all the minerals, and the mean size of the minerals was estimated from thin section observations of the bedrock samples. During the simulations, the clay mineral precipitation and the evolution of reactive surfaces of primary minerals are tracked together with chemical processes and water chemical composition. However, in view of the short time scales of transport renderer by the hydrological simulations (weekly to monthly timescale), the change in reactive surfaces of primary minerals became negligible. Precipitation of other secondary minerals such as carbonates, hematite or amorphous silica was tested, but these

minerals were not formed given the hydroclimatic context of the Strengbach catchment. The secondary mineral precipitation is therefore controlled by the formation of clay minerals. The KIRMAT code has already been applied in geochemical modeling of alluvial groundwaters (Lucas et al., 2010) and surface waters (Lucas et al., 2017; Ackerer et al., 2018).

For this study, the modeling strategy is adapted from Ackerer et al. (2018) to consider the new transit time and water mixing constrains provided by the hydrological code NIHM. To capture the chemical composition of the spring and the piezometer waters, numerical simulations were performed along the flow lines that were determined through the backtracking approach. A sketch of the hydrogeochemical modeling strategy is provided in figure 5. For each flow line, several KIRMAT simulations were performed with different starting positions along the active part of the line. The starting positions represent the locations at which the soil solutions percolate through the subsurface shallow aquifer. These variable starting positions are spaced with a constant distance along the flow line. The deepest soil solutions collected to the south of the catchment at the beech plot (HP) and to the north at the spruce plot (VP) were assumed representative of the soil solutions for the whole southern and northern slopes of the catchment, respectively. The data of the soil solution chemistry used in this study are available in Prunier et al. (2015) and in supplementary tables (tables EA6 and EA7). These soil solutions aggregate the effects of the various surface processes occurring before percolation into the bedrock. As the soil solution evolutions over time are monitored and injected as such into the modeled aquifer, the temporal variability of the soil solution chemistry and its repercussion on the water-rock interactions along the flow paths are taken into account by the modeling approach. Data related to the bedrock properties, such as the mineralogical compositions, the

mineral reactive surfaces, and the kinetic constants of dissolution reactions, are given in Ackerer et al. (2018) and in supplementary tables (tables EA10 to EA13). By following this strategy, the simulations that consider soil solutions percolating at the upper part of the catchment reflect the chemical evolution of waters with long path lengths and long transit times within the aquifer. By contrast, shorter path lengths and shorter transit times are associated with the percolation of soil solutions that occurs in the vicinity of the sampling locations (figure 5). Because the springs or the piezometers collect waters from different origins and with contrasted transit times, integration along each water flow line was performed. The aim of the integration is to determine the mean chemical composition resulting from the mixing of the waters characterized by variable transit times (figure 5). The integrated chemical composition of the waters provided by a given flow line is calculated by taking the arithmetic mean of the solute concentrations calculated by the succession of the KIRMAT simulations along the flow line (figure 5). This arithmetic mean reflects a simple full mixing of uniform water fluxes irrespective of their short or long transit times. In other words, the geochemical simulations are based on the hypothesis of spatially homogenous water-rock interactions within the watershed. The soil solutions are assumed to percolate uniformly within the aquifer and are then conveyed along the slopes by uniformly distributed mass of water until reaching the sampling locations.

4- Hydrological modeling results

4-1 Spatial variability of the flow lines

The results provided by the hydrological code NIHM show that to first order, the Strengbach catchment is well drained and that the topography exerts an important control on the flow line

distribution (figure 4). Along the hillsides with uniform or slightly convex slopes, the water flow lines show simple characteristics. The flow paths are nearly parallel, and the water velocities are similar along the different flow lines on this type of hillside. The water velocities tend to increase when moving downstream (longer traveled distances for a given transit duration, figure 4), with slower velocities near the main crests and higher velocities on the steepest parts of the hillsides. The waters collected along this type of hillside are therefore characterized by small variability of transit times. This is the case for the CS1, CS3 and RH3 spring waters located on the southern and northern parts of the catchment (figure 4). This is also the case for the piezometers PZ3 and PZ5 in the southern part of the watershed (figure 4). For the samplings located on uniform or slightly convex slopes (CS1, CS3, RH3, PZ3 and PZ5), the characteristics of the different flow lines that feed each site are therefore comparable for a given site and for a given date. By contrast, in the vicinity of the valley and in the topographic depressions, the hydrological modeling indicates that the flow line characteristics are more variable. Because flow lines coming from different hillsides can feed a topographic depression, the mixing of different flow lines with variable flow paths and contrasting water velocities can occur at these locations. The waters collected in valleys or in topographic depressions are therefore characterized by a higher variability of transit times. This is the case for the CS2 and CS4 springs, which are located in a depression in the axe of the small valley and surrounded by slopes with various orientations and a complex flow line distribution (figure 4). For these two springs, the characteristics of the different flow lines can be different for a given date.

4-2 Temporal variability of the flow lines

Hydrological modeling under general transient conditions can render the evolution over time of water flows in the Strengbach watershed but also of other hydraulic variables or parameters. As an example, after an important rainfall event (30/03/2010, in figure 6), snapshots of the average hydraulic conductivity in the subsurface show increasing values with decreasing elevation in the watershed. The same observation holds for hydraulic conductivity during drought periods (see 29/11/2011, in figure 6). Provided that the hydraulic head gradient is largely dominated by the topography and therefore almost constant over time (figure 6), the water velocities are increasing along the flow lines from crests to valleys, irrespective of the wet versus dry hydrological periods. For the CS1 spring, the mean flow velocities along the flow lines vary from approximately 1 m/day to 7 m/day between the severe drought of 29/11/2011 and the strong flood of 30/03/2010 (figures 7A and 7B). These events correspond to the annual maximum and minimum observed flow rates of the stream at the outlet of the Strengbach watershed. For the same dates, the mean velocities vary from 2 – 12 m/day, 1 – 4 m/day and 1 – 9 m/day for the springs CS2, CS3 and CS4, respectively. The variations from drought to flood are very similar for the piezometer waters, with velocities in the ranges 2 – 10 m/day and 2 – 12 m/day for the PZ3 and PZ5 piezometers, respectively. The RH3 spring located on a steeper part of the northern slopes exhibits flow velocity variations from 5 to 20 m/day from dry to flood conditions. In addition to the flow velocity variations, the hydrological simulations also reveal variability in the lengths of the active parts of the flow lines. Such variability is triggered by the particular seasonal variations of the hydraulic conductivities within the catchment. During periods of drought, the simulations indicate a strong decrease of hydraulic conductivities close to the main crests and much smaller variations at mid-slopes (figure 6). The crests rapidly dry out, whereas

the areas at mid-slopes still supply some water to the stream network. These contrasting hydrological behaviors result from the differences in aquifer thickness and water storage between the crests and the other parts of the catchment (figure 2). A thin aquifer, flow divergence and the absence of feeding areas prevent large water storage on the crests, in opposition to mid-slope parts with much thicker aquifers and the presence of feeding areas upstream. This particular pattern simulated for the hydraulic conductivities implies that the active parts of the flow lines extend up the main crests during important floods, whereas they are limited to mid-slopes after a long dry period. The consequence of this hydrological functioning is to moderate the seasonal variations of the transit times of waters, as the active lengths of flow lines vary simultaneously with water flow rates. Calculations indicate that for the spring and piezometer waters collected in this study, the mean transit times of waters only vary from approximately 1.75 to 4 months between the strongest flood and the driest conditions. These short subsurface water transit times are explained by the small size of the catchment and gravity driven flow along steep slopes.

5- Hydrogeochemical modeling results

Modeling the geochemical composition of waters from the different springs and piezometers selected for this study was performed following the procedure described in paragraph 3-2. The results are presented below by grouping sources and piezometers according to their hydrogeological characteristics.

5-1 CS1 and CS3 springs (southern slope)

The CS1 and CS3 springs emerge on the same slope and drain the same rocks. Their hydrological behavior is also very similar in terms of flow lines and water transit times. The interesting consequence of the simple flow line distribution for these springs is that a single flow line can be considered as representative of all the flow lines that are feeding the spring, irrespective of the hydrological conditions. Hydrogeochemical simulations were performed along a single flow line for different hydrological periods using the methodology illustrated in figure 5. The case of CS1 spring is used below to highlight the main results obtained from this approach. For the strong flood of 30/03/2010, the KIRMAT simulations modeling the waters coming from the proximity of the spring and characterized by short transit times produced too much diluted solutions, whereas the waters coming from the main crests are too much concentrated to reproduce the spring water chemical composition. However, after an integration of all the waters arriving at CS1 with the different transit times employed for the simulation, the resulting geochemical composition correctly reproduces the chemical composition of CS1 spring water at this date (H_4SiO_4, Na^+, K^+, Mg^{2+}, and Ca^{2+} concentrations, figure 7D). A similar conclusion is obtained for the important drought of 29/11/2011. Again, geochemical integration of all the waters arriving at CS1 along a water line but with different transit times correctly reproduces the chemical composition of the CS1 spring waters collected on this date (figure 7C). This is actually the case regardless of the time period considered. The coupled hydrological and hydrogeochemical approach has been applied for the CS1 spring for 6 dates covering the whole range of the water discharges of the spring (table 1). The modeling results reveal the seasonal variations of the water chemical composition of the CS1 spring over the whole range of observed flow rates at CS1 (figure 8). Simulations especially account for the 20-30% variation in H_4SiO_4 concentrations,

400 the 10-20% variation in Na^+ concentrations, and the relatively stability of the pH of the CS1
401 waters (figures 8A, 8C, 8D). The response in concentration of each chemical element to a
402 change in water discharge is associated with the initial soil solution concentrations, the nature
403 of primary minerals leached by water, and the degree of its incorporation into the clay solid
404 solutions. For example, Na is only provided by a single primary mineral (albite) and is weakly
405 incorporated into clays. Si is provided by several primary minerals (albite, biotite, K-feldspar, …)
406 and strongly incorporated in clays that are characterized by varying precipitation rates with
407 hydrological conditions. These points explain why the response of solute concentrations to
408 hydrological changes is variable for each element. Similar results are obtained for the CS3 spring
409 (figure EA1), showing, as for the CS1 spring, that the proposed modeling approach is able to
410 correctly capture the water chemical composition of the CS3 spring.

411 **5-2 PZ3 and PZ5 piezometers (southern slope)**

412 The two piezometers PZ3 and PZ5 are located on the southern part of the catchment, and their
413 waters drain granitic bedrock similar to that drained by the CS sources. As for the CS1 and CS3
414 springs, the NIHM modeling results show that the flow lines arriving at the PZ3 piezometer are
415 characterized by a relatively simple distribution. The flow lines are close to each other, and they
416 render similar water velocities on the slopes (figure 4). For the PZ5 piezometer located
417 downstream, the flow lines cover a larger area on the slope, especially during droughts (figure
418 4). However, for a given date, all the flow lines show similar velocities, with particularly fast
419 flows on a lower portion of the hillslope. These results imply that, as for the CS1 and CS3
420 springs, the hydrogeochemical simulations of PZ3 and PZ5 piezometer waters can be performed
421 by relying upon a single flow line representative of all the waters collected by the piezometers

422 on a given date. The geochemical integration along the flow line has been performed in the
423 same manner as detailed above, and this approach is able to reproduce the chemical
424 composition of the waters of the two piezometers, as illustrated in figure 9 for the flood of the
425 05/05/2015 and in figure EA2 for the dry conditions of 10/11/2015. Together, these modeling
426 results show that the linear or slightly convex slopes on the southern part of the catchment
427 allow to correctly capture the water chemistry of each sampling site with a straightforward
428 integration along a single and representative flow line.

429 **5-3 The CS2 and CS4 springs (in the valley axe)**

430 CS2 and CS4 spring waters drain the same granitic bedrock as the CS1 and CS3 waters, but are
431 located in the axe of the small valley of the Strengbach stream and surrounded by slopes of
432 various orientations and inclinations (figure 4). Consequently, the distribution of the flow lines is
433 much more scattered than for the CS1 and CS3 springs. The modeling strategy applied for these
434 two springs and the results are detailed below for the CS2 spring. For this spring, and for all the
435 hydrological conditions, two different groups of flow lines have been determined by the
436 backtracking approach: a northern group characterized by relatively slow velocities and a
437 southern group with higher velocities (figure 4). When the hydrological conditions vary from a
438 strong flood (30/03/2010) to an important drought (29/11/2011), the flow rates tend to
439 decrease along all the flow lines (figures 10A and 10B). For example, the mean flow velocities
440 along the flow lines vary from approximately 12 m/day to 2 m/day between these two dates.
441 However, for a given date, the northern group systematically renders slower velocities than the
442 southern group. This scattered distribution of the flow lines implies that a single specific flow
443 line cannot be representative of all the waters collected by the spring. The flow lines calculated

444 using the NIHM model allow for constraining the trajectories of the waters within the
445 watershed; however, the simulations performed in this study cannot provide the mass fluxes of
446 water carried by each flow line. Consequently, a straightforward calculation of the chemistry of
447 the CS2 spring, such as detailed above for CS1, is not applicable because the mixing proportions
448 between the different flow lines are unknown. Alternatively, it is possible to determine the
449 concentrations in the waters carried by the slowest and the fastest flow lines that are feeding
450 the spring and to compare the results with the observed chemistry of the spring water. The
451 results indicate that for all the hydrological conditions, the concentrations calculated from the
452 geochemical integration along the slowest and the fastest flow lines are able to correctly frame
453 the chemical composition in terms of H_4SiO_4, Na^+, K^+, Mg^{2+}, and Ca^{2+} of the CS2 spring waters
454 (results are presented for H_4SiO_4 and Na^+ in figures 10C and 10D). The observed chemistry of the
455 CS2 spring is bounded by the chemical compositions of the waters carried by the slowest and
456 fastest flow lines. The modeling results also suggest that the contributions of the slow and fast
457 flow lines are comparable over most of the hydrological conditions, as the observed
458 concentrations are in general at the midpoint between the min (i.e., fast) and max (i.e., slow)
459 boundaries (see figures 10C and 10D). It is only for the important droughts that the spring
460 chemistry seems to be mainly controlled by the southern and faster group of flow lines. Further
461 works to precisely estimate the mass fluxes of water carried by each flow line are necessary to
462 calculate the chemistry of the CS2 spring water with a weighted mixing calculation. The same
463 conclusions apply to the CS4 spring located in the proximity of CS2 spring.

464 **5-4 The RH3 spring (northern slope)**

The RH3 spring is located on the northern part of the catchment (figure 4), where steep slopes imply fast water velocities and subparallel flow lines. However, if the distribution of the flow lines on the RH3 hillside is simple (as for the CS1 and CS3 springs) the precise lithological nature of the bedrock drained by the RH3 waters is more difficult to constrain (see also Ackerer et al., 2018). Unlike the southern slope, the bedrock of the northern part of the catchment exhibits a complex lithology, with gneiss outcropping in the upper part of the slope and granite of variable degree of hydrothermal overprinting in the intermediate and lower parts. These lithological variations can explain the differences in chemical composition between the RH3 spring waters and the waters of the southern part of the catchment: the RH3 spring waters are characterized by systematically higher concentrations of K^+ and Mg^{2+} cations but show similar concentrations for the other major elements (Ackerer et al., 2018; Pierret et al., 2014). The vertical extension of the gneiss formation and the spatial variability of the hydrothermal overprinting along the northern slopes of the catchment are not very well known, which renders impossible the straightforward modeling of the RH3 spring water composition, as it was done for the CS1 and CS3 sources. Alternatively, simulations of two extreme cases can be performed by assuming that the flow lines only run, either on gneiss or on hydrothermally altered granite. When only considering the hydrothermally altered granite (VS facies), the simulated concentrations of H_4SiO_4 and Na^+ are close to the measured ones. However, the concentrations of K^+ and especially Mg^{2+} are clearly underestimated (figure 11B). In the case of the flow lines only running on gneiss (GN facies), the simulated concentrations of H_4SiO_4 and Na^+ also match the data. However, due to the higher abundance of biotite in the gneiss, the simulated concentrations of K^+ and Mg^{2+} are higher than the measured ones (figure 11A). At this stage, it is

therefore reasonable to propose that the chemical composition of the RH3 spring waters reflects mixing of the two lithological influences. By assuming a geochemical conservative mixing, which is likely a too simplistic scenario, the results would indicate that the flow lines portions running on gneiss and on hydrothermally altered granite count for approximately 40-50% and 50-60% of the total water path length, respectively. Further works to estimate the location of the contact between gneiss and granite are required for more realistic modeling and hence a deeper interpretation of the chemical composition of RH3 spring waters. In any case, the important point to stress here based on the above simulations is that the complex lithology and bedrock heterogeneity mainly impact the K^+ and the Mg^{2+} budget of the RH3 waters, but not or only slightly the H_4SiO_4 and Na^+ concentrations, which control the main part of global weathering fluxes carried by the Strengbach spring waters. These results readily explain why although the RH3 spring waters exhibits higher Mg^{2+} and K^+ concentrations than the other CS springs, they carry relatively similar global weathering fluxes (Viville et al., 2012; Ackerer et al., 2018).

6- Discussion

The modeling approach proposed in this study and based on the coupling of the NIHM and KIRMAT codes, allows for building a better modeling scheme than those commonly used in previous studies regarding the hydrogeochemical modeling of surface waters at the watershed scale. In such previous works, the geochemical simulations were performed mainly along a single 1D flow line, only characterized by homogeneous mean hydrological properties (Goddéris et al., 2006; Maher et al., 2011; Moore et al., 2012; Lucas et al., 2017; Ackerer et al., 2018). In the previous study on the Strengbach watershed (Ackerer et al., 2018), the soil solutions were

509 also assumed to percolate in the bedrock only at a single starting point of the flow lines.
510 Although these previous approaches were useful for determining the long-term evolution of
511 regolith profiles and/or the mean chemistry of waters at the multiyear scale, they cannot be
512 used to discuss the seasonal variations of the water chemical composition. The NIHM-KIRMAT
513 coupling approach makes this possible, as it provides the spatial distribution of the flow lines at
514 the watershed scale and their variations over time. Furthermore, the proposed modeling
515 approach also integrates a soil solution percolation scheme with inlets uniformly distributed
516 along the slope, which is more realistic than a scheme assuming that each sampled site is fed by
517 a single flow line carrying waters with a unique transit time. The consistency of the modeling
518 results with the measured concentrations over the whole range of the hydrological conditions
519 certainly gives weight to the application of the proposed modeling approach to the Strengbach
520 catchment. Such consistency also gives weight to the assumptions made regarding the
521 modeling parameters used in this work, i.e., reactive surfaces and kinetic constants. It also gives
522 weight to the conclusions and implications that can be deduced regarding the
523 hydrogeochemical functioning of the watershed, and the origin of the chemostatic character of
524 these waters. These different points are detailed below.

525 **6-1 Choices of the reactive surfaces and the kinetic constants**

526 For the geochemical simulations performed in this study, the kinetic constants that were used
527 to describe the dissolution reactions of the primary minerals are standard constants determined
528 through laboratory experiments (supplementary table EA12). The reactive surfaces of the
529 primary minerals were calculated by assuming a simple spherical geometry for all the minerals
530 (supplementary table EA10). Such choices might appear surprising as over the last years, several

studies have suggested that the kinetic constants determined through laboratory experiments overestimate the rates of the dissolution reactions in natural environments (White and Brantley, 2003; Zhu, 2005; Moore et al., 2012; Fischer et al., 2014). The origin of this laboratory-field discrepancy is still a matter of debate (Fischer et al., 2014). Different processes have been proposed to explain the gap between laboratory and field estimates, such as the crystallographic anisotropy (Pollet-Villard et al., 2016), progressive occlusion of the primary minerals by clays (White and Brantley, 2003), or the formation of passivation layers at the surfaces of the minerals (Wild et al., 2016; Daval et al., 2018). The difficulty to reconcile field and laboratory estimates can also be related to the challenge of defining relevant reactive surfaces at different space scales (Li et al., 2006; Navarre-Sitchler and Brantley, 2007). The present modeling work regarding the Strengbach catchment shows that the chemical composition variability of the spring and piezometer waters is fully captured via geometric reactive surfaces and standard kinetic constants, while respecting the water-rock interaction times within the catchment. This result suggests that the mean rates of the weathering reactions employed in this modeling work are realistic, which in turn implies that the modeling approach developed in this study does not underline significant mismatches between field and laboratory reaction rates. More details are given in the following to investigate why geometric reactive surfaces and standard kinetic constants are able to correctly capture the water chemistry. The calculated rates of the dissolution reactions depend on the product between the kinetic constants of the reactions and the mineral reactive surfaces. In the experimental studies performed for determining the kinetic constants of dissolution reactions, the constants are usually determined by normalizing the experimental weathering rates with the Brunauer-

553 Emmett-Teller surfaces determined from experiments of gas absorption (BET surfaces; Chou
554 and Wollast, 1986; Lundstrom and Ohman, 1990; Acker and Bricker, 1992; Amrhein and Suarez,
555 1992; Berger et al., 1994; Guidry and Mackenzie, 2003). In table 3, the BET surfaces are
556 compared with the geometric surfaces of the minerals involved in the dissolution experiments,
557 recalculated from the size ranges of the minerals. For most of the minerals (apatite, quartz,
558 albite, K-feldspar, and anorthite), the geometric surfaces are within the same order of
559 magnitude as the BET surfaces, even if often slightly lower (table 3). However, as the BET
560 surfaces are determined with fairly large uncertainties, especially for low BET surfaces (up to ±
561 70%), and as they can be very different depending on the gas used (up to 50% of difference
562 between N2 or Kr absorption; Brantley and Mellott, 2000), the above differences between the
563 geometrical and the BET surfaces cannot be considered significant for the majority of minerals
564 used in the Strengbach simulations. A significant difference only appears for biotite, with the
565 geometric surfaces one order of magnitude less than the BET surfaces (table 3). However, for
566 biotite, due to its layered structure, it has been shown that approximately 80 – 90% of the
567 surface area accessible by the gases used to estimate BET surfaces is not accessible for
568 weathering reactions (Nagy, 1995). In the case of biotite, the effective surface area for the
569 water-rock interactions would thus be, in a rather fortuitous manner, a surface area close to the
570 geometric one. The above considerations and observations thus explain why for a granitic
571 bedrock as found in the Strengbach catchment, the geometric surfaces are relevant to describe
572 the surfaces of water-rock interactions at the space and time scales of this study. An immediate
573 corollary is that the values of the standard kinetic constants (table EA12) are also appropriate to
574 calculate reaction rates with mineral geometric surfaces in our modeling approach. This ability

may be related to the fact that all the minerals that have been used in the dissolution experiments and in the kinetic studies were collected in the field (e.g., Acker and Bricker, 1992; Amrhein and Suarez, 1992). These minerals were likely affected by anisotropy, passivation layers, and any types of aging effects related to long-term water-rock interactions. Our results might therefore mean that the standard kinetic constants obtained in such experiments integrate the aging effects that have affected the reactivity of the primary minerals in natural environments. This would explain why it is possible to capture the full variability of the water chemistry in an elemental catchment with simple geometric reactive surfaces and standard kinetic constants. It is important to emphasize at this stage that the results of our simulation strengthen the idea that the low surfaces calculated from the geometrical shapes of minerals provide good estimates of the reactive surfaces within the natural environment (Brantley and Mellott, 2000; Gautier et al., 2001; White and Brantley, 2003; Zhu, 2005; Li et al., 2017). They are certainly the values to be used for hydrogeochemical modeling such as that performed in this work, in addition to the use of the experimental kinetic constants for mineral dissolution. These conclusions are certainly not specific to the Strengbach catchment and could be applicable to many other granitic catchments.

6-2 Implications for the acquisition of the water chemistry

The results of the NIHM-KIRMAT hydrogeochemical modeling have strong implications regarding the hydrogeochemical functioning of the Strengbach watershed. The NIHM modeling shows that the hydrological functioning of the watershed is correctly simulated by water circulations in the shallow subsurface, i.e., in a saprolitic aquifer. No contribution of waters circulating in the deep fracture network of the granitic bedrock and observed during the drilling

campaigns is necessary. The deep-water circulation pathways are probably disconnected from the shallow subsurface, or with mean hydraulic heads less than those of the subsurface, at least at the Strengbach catchment scale, and does not significantly impact the water budget of the Strengbach catchment. As detailed in section 4-1, the modeling results show that water in the shallow aquifer flows along streamlines with fairly simple geometries. At the scale of the watershed (figure 4), the geometry of the flow lines validates the hypothesis built on the basis of the geochemical and Sr-U isotopic data that the spring waters of these mid-mountain basins (i.e., the Ringelbach and Strengbach watersheds; Schaffhauser et al., 2014; Pierret et al., 2014) are supplied by waters from distinct flow paths without real interconnections. More importantly, the modeling results emphasize the importance of water transit times within the watershed as a main feature controlling the chemical composition of subsurface waters at the Strengbach catchment. Along all the slopes, the waters coming from the proximity of the crests and characterized by a long transit time systematically render higher concentrations than the waters with shorter pathways and transit times. When the hydrological conditions change from wet to dry periods, the solute concentrations also tend to increase with the increase in the mean transit time of waters. Our results demonstrate in particular that for the CS1 source and for the PZ3 and PZ5 piezometers, all located on the southern slope of the watershed, over a homogeneous granitic bedrock, and all characterized by flow lines of fairly simple geometries (section 4), the spatial and temporal variations of their geochemical composition are fully explained by differences in water residence times (figure 12). Residence time variations between high and low discharge periods explain the temporal variations of geochemical signatures within each site, and the differences in mean residence times of waters supplying the

619 different sources and piezometers explain the various chemical compositions between the
620 different sites (figure 12). Only the CS2 and CS4 springs, located in a depression, are supplied by
621 two different types of water flow lines, the contribution of which could change over time.
622 However, the mixing of different flow lines has probably a relatively modest impact, and at the
623 scale of the watershed, the results show that the duration of water-rock interaction exerts a
624 first-order control on the chemical composition of waters, in addition to the lithological
625 parameter. This study brings also strong constrains on the spatial repartition of the weathering
626 processes. For the modeling strategy developed in this study, the chemical composition of the
627 spring and piezometer waters are calculated by integrating the chemical composition of waters
628 introduced at different starting positions along the active part of the flow lines (figure 5). In
629 each of the simulations, a fixed distance between the initial positions of the KIRMAT simulations
630 along the flow lines was used. The modeling results show that through the geochemical
631 integration, the concentrated waters coming from the main crests are naturally
632 counterbalanced by the diluted waters infiltrating close to the sampling sites. From flood to
633 drought events, the mean transit times are obviously impacted by the variable velocities along
634 the flow lines, but regardless of the hydrological conditions, it is always possible to explain the
635 water chemistry of the sampling sites with the above integration scheme. Such repeatable
636 consistency between data and simulations indicates that this circulation scheme is certainly
637 quite realistic for the Strengbach catchment. This scheme supports the idea suggested in
638 Ackerer et al. (2016) that at the scale of the watershed, the solute chemistry is acquired through
639 reactions and weathering processes that are spatially relatively homogenous within the
640 watershed.

6-3- Origin of the chemostatic behavior in the Strengbach catchment

The hydrogeochemical monitoring of the spring, piezometer, and stream waters performed in the Strengbach catchment clearly shows that this catchment has a chemostatic behavior (e.g., Viville et al., 2012; Ackerer et al., 2018; this study). All the spring and the piezometer waters have chemical concentrations impacted by changes in the hydrological conditions, but the concentration variation ranges are by far narrower than variation ranges of water discharges, which define the chemostatic behavior of a hydrological system. For the waters exhibiting the largest concentration variations (spring CS1), a moderate increase of approximately 10-30% in the concentrations of H4SiO4 and Na+ is observed from floods to severe drought events, while the water discharges may vary by a factor of 15 (figures 8A and 8C). This weak variability of the solute concentrations over a wide range of water discharges is not specific to the Strengbach catchment; it has rather been observed in several watersheds spanning different climates and hydrological contexts (Godsey et al., 2009; Clow and Mast, 2010; Kim et al., 2017). Different origins for the chemostatic behavior have been proposed, such as a modification of the mineral reactive surfaces during changing hydrological conditions (Clow and Mast, 2010), a small concentration difference between slow and fast moving waters (Kim et al., 2017), or the fact of reaching an equilibrium concentration along the water pathway (Maher, 2010). To date, the study of concentration-discharge relationships has been intensively used to assess the chemostatic behavior of waters (Godsey et al., 2009; Kim et al., 2017; Ameli et al., 2017). However, the lack of precise estimates of water transit times limits the ability to clearly discuss the origin of the chemostatic behavior on the single basis of the concentration-discharge relationships. The coupled approach presented in this study offers a renewed opportunity to

663 discuss the origin of the chemostatic behavior in catchments because the acquisition and the
664 evolution of the water chemistry can be simulated along flow lines determined via timely and
665 spatially distributed hydrological modeling. The strength of this approach is to constrain water
666 transit times independently and before any geochemical simulation.

667 The results from the hydrological model show that the characteristics of the flow lines are
668 affected by the changes in the hydrological conditions. After important precipitations, high
669 water contents and large hydraulic conductivities (as the local mean value integrated over the
670 aquifer thickness including the vadose and saturated zones) are simulated in the vicinity of the
671 crests and all along the small valley of the catchment (figure 6). During drought periods, the
672 crest lines have progressively dried out, and the hydraulic conductivities strongly decrease on
673 the upper parts of the watershed. Only some locations at mid-slopes and along the direction of
674 the principal valley exhibit modest hydraulic conductivities (figure 6). This response of the
675 hydraulic conductivities implies that during floods, the water velocity significantly increases
676 along the flow lines, but the length of the active parts of the flow lines also increase as waters
677 collected downstream may also come from the neighborhood of the main crests. During
678 drought periods, the water velocity is slower, but the length of the active parts of the flow lines
679 also tends to decrease, as the waters are principally supplied by mid-slope areas characterized
680 by a thicker aquifer. For illustration, and for the CS1 spring, the water velocities varied along the
681 flow lines between 7 and 0.5 m/day during the flood of 30/03/2010 and were approximately
682 0.5-1 m/day during the important drought of the 29/11/2011 (figure 6). At the same time, the
683 active parts of the flow lines were reduced from 160 m to 110 m from the flood to the drought
684 events (figures 7A and 7B). This hydrological functioning implies that the water velocities along

685 the flow lines and the active lengths of the flow lines vary in opposite manners from drought to
686 flood events. This hydrological behavior buffers the variations of the water transit times over
687 changing hydrological conditions and explains why the mean transit times span much narrower
688 variation ranges than the discharges of water at the collected springs. For example, the
689 calculated mean transit times of waters for the CS1 spring vary from 1.75 to 3.13 months
690 between the strongest flood and the driest period that have been studied, whereas the water
691 discharges vary from 1.523 L/s to 0.098 L/s (figure 8B). Because the time of the water-rock
692 interactions exerts a first-order control on the chemical composition of waters, the modest
693 variability of the mean transit times is directly responsible for the relative stability of the
694 chemical composition of waters within the catchment.

695 It is worth noting that the hydrological modeling with the NIHM code is performed
696 independently and before any geochemical simulation with the KIRMAT code. The fact that the
697 flow rates are well reproduced for all the hydrological contexts between 2010 and 2015
698 supports the idea that water transit times inferred with NIHM are realistic. With chemical
699 composition of waters well captured by simulations, the combination of the geochemical
700 parameters used in KIRMAT renders realistic reaction rates, as chemistry is well reproduced
701 while respecting water transit times. No modifications of the reactive surfaces and of the
702 dissolution kinetic constants were necessary to reproduce the seasonal variability of the water
703 chemistry. It is also important to emphasize that the simulated chemical compositions of waters
704 remain far from a state of chemical equilibrium with respect to primary minerals. The calculated
705 Gibbs free energy for the primary minerals ranges from -120 to -100 kJ/mol for apatite, -90 to -
706 80 kJ/mol for biotite and anorthite and -30 to -20 kJ/mol for albite and K-feldspar. These far-

from-equilibrium values for the Gibbs free energy imply that the reaction rates calculated using hydrogeochemical codes such as KIRMAT, which are based on the transient state theory (TST, Eyring, 1935; Murphy and Helgeson, 1987), are realistic for most of the primary minerals in this type of hydrological context. Regarding the simulations performed in this study, the relatively short residence times of waters and the precipitation of clay minerals prevent reaching a state of chemical equilibrium between waters and primary minerals. The results also indicate that introducing a clay solid solution in the geochemical system is a good way to capture the clay mineral dynamics, with a solid solution precipitated at thermodynamic equilibrium able to generate reliable water chemistry (this study) and realistic clay precipitation rates (more detail in Ackerer et al., 2018). Further development could consider a more precise approach to the formation of the clay phases but would imply to simulate a kinetically-controlled nucleation and growth of clay particles (Fritz et al., 2009, Noguera et al., 2011). Further comparisons facing the results from the hydrological modeling with water isotope variability could also be interesting to discuss the accuracy of the water transit times inferred by simulations. Taken together, the results of this study show that the solute concentrations are not limited by a chemical equilibrium; they simply are weakly variable over time because of the short and moderately variable water residence times in the watershed. The chemostatic behavior of the surface and the shallow subsurface waters is therefore only due to a strong hydrological control of the water transit times within the watershed. This conclusion could probably extend to other mountainous and relatively steep watersheds, in which water pathways and short transit times are mainly controlled by gravity driven flow along slopes.

7- Conclusion

This study emphasizes the potential of coupling low-dimensional and depth-integrated hydrological modeling with hydrogeochemical modeling as a way to better understand variability over time and space of the composition of surface and subsurface waters. The independent estimation of the water transit times provided by hydrological simulations is a clear added value to constrain the geochemical modeling approaches. This study shows that the durations of water-rock interactions exert a first-order control on the chemical composition of waters and that the acquisition of the water chemistry can be explained by weathering processes that are spatially fairly homogeneous over the catchment. The hydrological functioning of the watershed also indicates that the chemostatic behavior of the water chemistry is a direct consequence of the strong control exerted by hydrological processes on water transit times. The variations in flow lines distributions from drought to flood events result in a moderate seasonal variability of mean water transit times, which in turn explains the relative stability of the solute concentrations in waters. The consistency between measured and modeled concentrations while respecting the water-rock interaction times provided by the hydrological simulations shows that it is possible to capture the chemical composition of waters with simply determined reactive surfaces and standard kinetic constants. The results of our simulations strengthen the idea that the low surfaces calculated from the geometrical shapes of minerals are a good estimate of the reactive surfaces within the natural environment and certainly the values to be used for hydrogeochemical modeling such as that performed in this work, in addition to the use of the experimental kinetic constants for mineral dissolution.

Acknowledgements: This work and the Julien Ackerer's salary were financially supported by the French ANR Program (Project CANTARE- Alsace) under grant agreement ANR-15-CE06-0014.

This work also benefited from fruitful discussions with D. Daval and from very constructive reviews by anonymous reviewers.

Bibliography

Acker, J. G. and Bricker, O. P.: The influence of pH on biotite dissolution and alteration kinetics at low temperature. *Geochim. Cosmochim. Acta*, *56*(8), 3073-3092, 1992.

Ackerer, J., Chabaux, F., Van der Woerd, J., Viville, D., Pelt, E., Kali, E., Lerouge, C., Ackerer, P., Di Chiara Roupert, R. and Négrel, P.: Regolith evolution on the millennial timescale from combined U–Th–Ra isotopes and in situ cosmogenic 10Be analysis in a weathering profile (Strengbach catchment, France). *Earth Planet. Sci. Lett., 453*, 33-43, 2016.

Ackerer, J., Chabaux, F., Lucas, Y., Clément, A., Fritz, B., Beaulieu, E Viville D., Pierret, M.C., Gangloff, S. and Négrel, P.: Monitoring and reactive-transport modeling of the spatial and temporal variations of the Strengbach spring hydrochemistry. *Geochim. Cosmochim. Acta*, *225*, 17-35, 2018.

Ameli, A. A., Beven, K., Erlandsson, M., Creed, I. F., McDonnell, J. J. and Bishop, K.: Primary weathering rates, water transit times, and concentration-discharge relations: A theoretical analysis for the critical zone. *Water Resour. Res.*, *53*, 942-960, 2017.

Amrhein, C. and Suarez, D. L.: Some factors affecting the dissolution kinetics of anorthite at 25 C, *Geochim. Cosmochim. Acta*, *56*, 1815-1826, 1992.

Beaulieu, E., Goddéris, Y., Donnadieu, Y., Labat, D. and Roelandt, C.: High sensitivity of the continental-weathering carbon dioxide sink to future climate change, *Nature Climate Change*, *2*, 346, 2012.

Beaulieu, E., Lucas, Y., Viville, D., Chabaux, F., Ackerer, P., Goddéris, Y. and Pierret, M. C. : Hydrological and vegetation response to climate change in a forested mountainous catchment, *Modeling Earth Systems and Environment*, *2*, 191, 2016.

Beisman, J. J., Maxwell, R. M., Navarre-Sitchler, A. K., Steefel, C. I., & Molins, S. ParCrunchFlow: an efficient, parallel reactive transport simulation tool for physically and chemically heterogeneous saturated subsurface environments. *Computational Geosciences*, *19*, 403-422, 2015.

779 Berger, G., Cadore, E., Schott, J. and Dove, P. M.: Dissolution rate of quartz in lead and sodium
780 electrolyte solutions between 25 and 300 C: Effect of the nature of surface complexes and
781 reaction affinity, *Geochim. Cosmochim. Acta*, *58*, 541-551, 1994.
782 Brantley, S. L. and Mellott, N. P.: Surface area and porosity of primary silicate minerals, *Am. Mineral.*, *85*,
783 1767-1783, 2000.
784 Camporese, M., Paniconi, C., Putti, M. and Orlandini, S.: Surface-subsurface flow modeling with path-
785 based runoff routing, boundary condition-based coupling, and assimilation of multisource
786 observation data, Water Resour. Res. 46, W02512, *doi:10.1029/2008WR007536, 2010.*
787 Chabaux, F., Viville, D., Lucas, Y., Ackerer, J., Ranchoux, C., Bosia, C, Pierret, M.C., Labasque, T., Aquilina,
788 L., Wyns, R., Lerouge, C., Dezaye, C. and Négrel, P.: Geochemical tracing and modeling of surface
789 and deep water–rock interactions in elementary granitic watersheds (Strengbach and Ringelbach
790 CZOs, France), *Acta Geochim.*, *36*, 363-366, 2017.
791 Chou, L., and Wollast, R.: Steady-state kinetics and dissolution mechanisms of albite. *Am. J. Science*, *285*,
792 963-993, 1985.
793 Clow, D. W. and Mast, M. A.: Mechanisms for chemostatic behavior in catchments: implications for CO2
794 consumption by mineral weathering, *Chem. Geol.*, *269*, 40-51, 2010.
795 Daval, D., Calvaruso, C., Guyot, F. and Turpault, M. P.: Time-dependent feldspar dissolution rates
796 resulting from surface passivation: Experimental evidence and geochemical implications. *Earth*
797 *Planet. Sci. Lett.*, *498*, 226-236, 2018.
798 Ebel, B. A. and Loague, K.: Physics-based hydrologic-response simulation: Seeing through the fog of
799 equifinality. *Hydrological Processes: An International Journal*, *20*, 2887-2900, 2006.
800 Eyring, H. The activated complex in chemical reactions. *The Journal of Chemical Physics*, *3*, 107-115,
801 1935.
802

803 Fichter, J., Turpault, M. P., Dambrine, E. and Ranger, J.: Mineral evolution of acid forest soils in the
804 Strengbach catchment (Vosges mountains, NE France), *Geoderma*, *82*, 315-340, 1998.
805 Fischer, C., Kurganskaya, I., Schäfer, T. and Lüttge, A.: Variability of crystal surface reactivity: What do we
806 know?, *Applied Geochem. 43*, 132-157, 2014.
807 Fritz, B., Clément, A., Amal, Y. and Noguera, C.: Simulation of the nucleation and growth of simple clay
808 minerals in weathering processes : the NANOKIN Code, Geochim. Cosmochim. Acta, 73, 1340-
809 1358, 2009.
810 Gangloff, S., Stille, P., Schmitt, A.D. and Chabaux F.: Factors controlling the chemical composition of
811 colloidal and dissolved fractions in soil solutions and the mobility of trace elements in soils,
812 Geochim. Cosmochim. Acta, 189 37–57, 2016.
813 Gangloff, S., Stille, P., Pierret, M. C., Weber, T. and Chabaux, F. : Characterization and evolution of
814 dissolved organic matter in acidic forest soil and its impact on the mobility of major and trace
815 elements (case of the Strengbach watershed), *Geochim. Cosmochim. Acta*, *130*, 21-41, 2014.
816 Gautier, J. M., Oelkers, E. H. and Schott, J.: Are quartz dissolution rates proportional to BET surface
817 areas?, *Geochim. Cosmochim. Acta*, *65*, 1059-1070, 2001.
818 Gérard, F., Clément, A. and Fritz, B.: Numerical validation of a Eulerian hydrochemical code using a 1D
819 multisolute mass transport system involving heterogeneous kinetically controlled reactions, *J.*
820 *Cont. Hydrol.*, *30*, 201-216, 1998.
821 Gh'Mari, E. : *Etude minéralogique, pétrophysique et géochimique de dynamique d'altération d'un granite*
822 *soumis aux dépôts atmosphériques acides (bassin versant du Strengbach, Vosges, France).*
823 *Mécanismes, bilans et modélisation*, PhD Thesis,, Université Louis Pasteur, Strasbourg, pp. 200.
824 Gislason, S. R., Oelkers, E. H., Eiriksdottir, E. S., Kardjilov, M. I., Gisladottir, G., Sigfusson, B., Snorrason, A.,
825 Elefsen, S., Hardardottir, J., Torssander, P. and Oskarsson, N.: Direct evidence of the feedback
826 between climate and weathering, *Earth Planet. Sci. Lett.*, *277*, 213-222, 2009.

827 Goddéris, Y., François, L. M., Probst, A., Schott, J., Moncoulon, D., Labat, D. and Viville, D.: Modelling
828 weathering processes at the catchment scale: the WITCH numerical model, Geochim.
829 Cosmochim. Acta 70, 1128–1147, 2006.

830 Goddéris, Y., Brantley, S. L., François, L., Schott, J., Pollard, D., Déqué, M. and Dury, M.: Rates of
831 consumption of atmospheric CO_2 through the weathering of loess during the next 100 yr of
832 climate change, *Biogeosciences*, *10*, 135-148, 2013.

833 Godsey, S. E., Kirchner, J. W., and Clow, D. W.: Concentration–discharge relationships reflect chemostatic
834 characteristics of US catchments. *Hydrological Processes: An International Journal*, *23*, 1844-
835 1864, 2009.

836 Guidry, M. W. and Mackenzie, F. T.: Experimental study of igneous and sedimentary apatite dissolution:
837 control of pH, distance from equilibrium, and temperature on dissolution rates, *Geochim.*
838 *Cosmochim. Acta*, *67*, 2949-2963, 2003.

839 Gunduz, O. and Aral, M. M.: River networks and groundwater flow: a simultaneous solution of a coupled
840 system, *J. Hydrol.*, *301*, 216-234, 2005.

841 Gupta, H.V., Kling, H., Yilmaz, K.K., Martinez, G.F. Decomposition of the mean squared error and NSE
842 performance criteria: Implications for improving hydrological modelling. J. Hydrol. 377, 80–91,
843 2009.

844 Hazenberg, P., Broxton, P., Gochis, D., Niu, G. Y., Pangle, L. A., Pelletier, J. D., ... and Zeng, X. (2016).
845 Testing the hybrid-3-D hillslope hydrological model in a controlled environment, *Wat. Resour.*
846 *Res.*, *52*, 1089-1107, 2016.

847 Jeannot, B., Weill, S., Eschbach, D., Schmitt, L. and Delay, F.: A low-dimensional integrated subsurface
848 hydrological model coupled with 2-D overland flow: Application to a restored fluvial
849 hydrosystem (Upper Rhine River–France), J. Hydrol., 563, 495-509, 2018.

Kampf, S. K. and Burges, S. J.: A framework for classifying and comparing distributed hillslope and catchment hydrologic models, *Water Resour. Res.*, W05423, doi:10.1029/2006WR005370, 2007

Kim, H., Dietrich, W. E., Thurnhoffer, B. M., Bishop, J. K. and Fung, I. Y.: Controls on solute concentration-discharge relationships revealed by simultaneous hydrochemistry observations of hillslope runoff and stream flow: The importance of critical zone structure, *Water Resour. Res.*, *53*, 1424-1443, 2017.

Kirchner, J. W.: Getting the right answers for the right reasons: Linking measurements, analyses, and models to advance the science of hydrology, *Water Resour. Res. 42,* W03S04, doi:10.1029/2005WR004362, 2006.

Lebedeva, M. I. and Brantley, S. L. : Exploring geochemical controls on weathering and erosion of convex hillslopes: Beyond the empirical regolith production function. *Earth Surface Processes and Landforms*, *38*, 1793-1807, 2013.

Li, D. D., Jacobson, A. D. and McInerney, D. J.: A reactive-transport model for examining tectonic and climatic controls on chemical weathering and atmospheric CO2 consumption in granitic regolith. *Chem. Geol.*, *365*, 30-42 2014.

Li, L., Peters, C. A. and Celia, M. A.: Upscaling geochemical reaction rates using pore-scale network modeling. *Advances in water resources*, *29*, 1351-1370, 2006.

Li, L., Bao, C., Sullivan, P. L., Brantley, S., Shi, Y., & Duffy, C. Understanding watershed hydrogeochemistry: 2. Synchronized hydrological and geochemical processes drive stream chemostatic behavior. *Water Resources Research*, *53*, 2346-2367, 2017.

Li, L., Maher, K., Navarre-Sitchler, A., Druhan, J., Meile, C., Lawrence, C., ... and Jin, L. : Expanding the role of reactive transport models in critical zone processes. *Earth-Science Reviews*, *165*, 280-301, 2017

873 Lucas, Y., Schmitt, A. D., Chabaux, F., Clément, A., Fritz, B., Elsass, P. and Durand, S.: Geochemical tracing
874 and hydrogeochemical modelling of water–rock interactions during salinization of alluvial
875 groundwater (Upper Rhine Valley, France), *Appl. Geochem.*, *25*, 1644-1663, 2010.

876 Lucas, Y., Chabaux, F., Schaffhauser, T., Fritz, B., Ambroise, B., Ackerer, J. and Clément, A.:
877 Hydrogeochemical modeling (KIRMAT) of spring and deep borehole water compositions in the
878 small granitic Ringelbach catchment (Vosges Mountains, France), *Applied Geochemistry*, *87*, 1-
879 21, 2017.

880 Lundström, U. and Öhman, L. O.: Dissolution of feldspars in the presence of natural, organic solutes,
881 *Journal of Soil Science*, *41*, 359-369, 1990.

882 Maher, K., Steefel, C. I., White, A. F., & Stonestrom, D. A.: The role of reaction affinity and secondary
883 minerals in regulating chemical weathering rates at the Santa Cruz Soil Chronosequence,
884 California, *Geochim. Cosmochim. Acta*, *73*, 2804-2831, 2009.

885 Maher, K. : The dependence of chemical weathering rates on fluid residence time, *Earth Planet. Sci. Lett.*,
886 *294*, 101-110, 2010.

887 Maher, K.: The role of fluid residence time and topographic scales in determining chemical fluxes from
888 landscapes, *Earth Planet. Sci. Let.*, *312*, 48-58, 2011.

889 Mirus, B. B., Ebel, B. A., Heppner, C. S. and Loague, K.: Assessing the detail needed to capture rainfall-
890 runoff dynamics with physics-based hydrologic response simulation, *Water Resour. Res.*, *47*,
891 W00H10, doi:10.1029/2010WR009906, 2011

892 Moore, J., Lichtner, P. C., White, A. F. and Brantley, S. L.: Using a reactive transport model to elucidate
893 differences between laboratory and field dissolution rates in regolith, *Geochim. Cosmochim.*
894 *Acta*, *93*, 235-261, 2012.

Murphy, W. M., & Helgeson, H. C. Thermodynamic and kinetic constraints on reaction rates among minerals and aqueous solutions. III. Activated complexes and the pH-dependence of the rates of feldspar, pyroxene, wollastonite, and olivine hydrolysis. *Geochimica et Cosmochimica Acta*, *51*, 3137-3153, 1987.

Nagy. K. L.. White. A. F.. & Brantley. S. L. Chemical weathering rates of silicate minerals. *Mineralogical Society of America. Washington. DC*. 1995.

Navarre-Sitchler, A. and Brantley, S.: Basalt weathering across scales, *Earth and Planet. Sci. Let.*, *261*, 321-334, 2007.

Navarre-Sitchler, A., Steefel, C. I., Yang, L., Tomutsa, L. and Brantley, S. L.: Evolution of porosity and diffusivity associated with chemical weathering of a basalt clast, *Journal of Geophysical Research: Earth Surface*, *114*, F02016, doi:10.1029/2008JF001060, 2009.

Ngo, V. V., Delalande, M., Clément, A., Michau, N. and Fritz, B.: Coupled transport-reaction modeling of the long-term interaction between iron, bentonite and Callovo-Oxfordian claystone in radioactive waste confinement systems., *Applied Clay Science*, *101*, 430-443, 2014

Noguera, C., Fritz, B. and Clément, A.: Simulation of the nucleation and growth of clay minerals coupled with cation exchange, Geochim. Cosmochim. Acta, 75, 3402-3418, 2011.

Pan, Y., Weill, S., Ackerer, P. and Delay, F.: A coupled stream flow and depth-integrated subsurface flow model for catchment hydrology, *Journal of Hydrology*, *530*, 66-78, 2015

Pierret, M. C., Stille, P., Prunier, J., Viville, D. and Chabaux, F. : Chemical and U–Sr isotopic variations in stream and source waters of the Strengbach watershed (Vosges mountains, France). *Hydrology and Earth System Sciences*, *18*, 3969-3985, 2014.

Pollet-Villard, M., Daval, D., Ackerer, P., Saldi, G. D., Wild, B., Knauss, K. G. and Fritz, B.: Does crystallographic anisotropy prevent the conventional treatment of aqueous mineral reactivity? A

case study based on K-feldspar dissolution kinetics, *Geochim. Cosmochim. Acta*, *190*, 294-308, 2016.

Prunier, J., Chabaux, F., Stille, P., Gangloff, S., Pierret, M. C., Viville, D. and Aubert, A. : Geochemical and isotopic (Sr, U) monitoring of soil solutions from the Strengbach catchment (Vosges mountains, France): Evidence for recent weathering evolution, *Chem. Geol.*, *417*, 289-305, 2015.

Schaffhauser, T., Chabaux, F., Ambroise, B., Lucas, Y., Stille, P., Reuschlé, T., Perrone, T. and Fritz, B.: Geochemical and isotopic (U, Sr) tracing of water pathways in the granitic Ringelbach catchment (Vosges Mountains, France), *Chem. Geol.*, *374*, 117-127, 2014.

Schmitt, A.D., Gangloff, S., Labolle, F., Chabaux, F. and Stille, P.: Ca biogeochemical cycle at the beech tree - soil solution interface from the Strengbach CZO (NE France): insights from stable Ca and radiogenic Sr isotopes, Geochim. and Cosmochim. Acta 213, 91-109, 2017

Schmitt AD, Borrelli N., Ertlen D., Gangloff S., Chabaux, F. and Osterrieth M.: Stable calcium isotope speciation and calcium oxalate production within beech tree (Fagus sylvatica L.) organs, Biogeochemistry, 137,197-217, DOI 10.1007/s10533-017-0411-0, 2018.

Steefel, C. I., DePaolo, D. J. and Lichtner, P. C.: Reactive transport modeling: An essential tool and a new research approach for the Earth sciences, *Earth Planet. Sci. Let.*, *240*, 539-558, 2005

Tardy, Y. and Fritz, B.: An ideal solid solution model for calculating solubility of clay minerals, *Clay minerals*, *16*, 361-373, 1981.

Viville, D., Chabaux, F., Stille, P., Pierret, M. C. and Gangloff, S.: Erosion and weathering fluxes in granitic basins: the example of the Strengbach catchment (Vosges massif, eastern France), *Catena*, *92*, 122-129, 2012.

Weill, S., Altissimo, M., Cassiani, G., Deiana, R., Marani, M. and Putti, M.: Saturated area dynamics and streamflow generation from coupled surface–subsurface simulations and field observations, *Advances in water resources*, *59*, 196-208, 2013.

Weill, S., Delay, F., Pan, Y. and Ackerer, P.: A low-dimensional subsurface model for saturated and unsaturated flow processes: ability to address heterogeneity, *Computational Geosciences*, *21*, 301-314, 2017.

White, A. F. and Brantley, S. L.: The effect of time on the weathering of silicate minerals: why do weathering rates differ in the laboratory and field?, *Chem. Geol.*, *202*, 479-506, 2003.

Wild, B., Daval, D., Guyot, F., Knauss, K. G., Pollet-Villard, M. and Imfeld, G.: pH-dependent control of feldspar dissolution rate by altered surface layers, *Chemical Geology*, *442*, 148-159, 2016

Zhu, C.: In situ feldspar dissolution rates in an aquifer, *Geochim. Cosmochim. Acta*, *69*, 1435-1453, 2005

952 **Figure captions**

953 Figure 1: sampling locations within the Strengbach catchment. Blue stars represent springs, blue
954 diamonds represent piezometers, and the blue circle represents the stream at the outlet of the
955 watershed. Green circles represent soil solution locations, and black diamonds represent
956 bedrock facies locations.

957 Figure 2: on the left: field of thicknesses of the weathered material constituting the shallow
958 unconfined aquifer at the Strengbach catchment used for the simulations of NIHM. The 1D
959 surface draining network used in NIHM is represented by the black lines. On the right: fitting
960 observed flow rates from the Strengbach stream at the outlet of the catchment with simulations
961 of flow within the watershed (illustrated from 2010 to 2015). The subsurface compartment
962 inherits from the aquifer thicknesses reported in the left panel, and the topography makes the
963 natural outlet of the subsurface compartment the surface draining network.

964 Figure 3: principle of the method of backtracking used to determine flow lines that generate
965 flow at the outlet of the Strengbach catchment. Particles are dispatched along the dry fraction
966 of the 1D river network (only one is represented here at a position *a* on 01/01/2010 at 23:59).
967 NIHM generates an output heterogeneous velocity field at that date for the whole watershed,
968 denoted $V_{01/01/2010}$. By applying a velocity field of the same magnitude but opposite direction to
969 the particle, the position of the particle can be backtracked until 31/12/2009 23:59. Then, to
970 further backtrack the trajectory of the particle, the velocity field is updated accordingly. The
971 frequency of updating of the velocity field was set to 1 day, as a compromise between the
972 accuracy of results and computational time considerations.

973 Figure 4: at the top, flow lines of the subsurface that feed with water the surface draining
974 network on March 1st, 2010 (on the left, high-flow period) and July 1st, 2010 (on the right, low-
975 flow period). The color scale indicates that a water particle reaching the river at a given date
976 started its travel along the streamline or passed at a given location on the streamline x days
977 before. The density of streamlines is associated with the flowing versus dry fraction of the river
978 network at a prescribed date. Below, flow lines of the subsurface that feed with water the
979 geochemical sampling sites on March 30th, 2010 (on the left, flood event) and November 29th,
980 2011 (right, drought event) according to NIHM simulations. For each sampling site, 10 particles
981 were dispatched in the direct neighborhood of the site and then backtracked. The color scale
982 indicates that a water particle reaching the sampling site at a given date started its travel along
983 the streamline or passed at a given location on the streamline x days before.

984 Figure 5: conceptual scheme used in the modeling of the water chemistry. The soil solutions are
985 used as input solution. The bedrock is discretized into a 1D succession of cells along the active
986 parts of the flow lines previously determined by the hydrological NIHM model. Within each cell,
987 the geochemical and transport equations are numerically solved using the KIRMAT
988 hydrogeochemical code. To calculate the integrated chemical composition of the spring water,
989 several simulations with different entering points of soil solutions along the flow path were
990 performed, and the integrated chemistry was calculated by taking the arithmetic mean of all the
991 simulated solute concentrations.

992 Figure 6: maps of piezometric gradient and mean hydraulic conductivity for the Strengbach
993 catchment, as simulated by NIHM, on 29/11/2011 (dry period) and 30/03/2010 (high flows

994 period). The mean hydraulic conductivity is the mean of all hydraulic conductivities integrated
995 over the depth of the aquifer and thus depends on the water saturation.

996 Figure 7: simulation results for the CS1 spring for an important drought (29/11/2011) and a
997 strong flood event (30/03/2010). At the top, active parts of the flow lines that bring the waters
998 to the CS1 spring for the two sampling dates (7A and 7B). Below, simulated chemical
999 compositions of the CS1 spring waters after integration along the flow lines and comparison
1000 with the initial soil solution and the spring chemistry data (7C and 7D). Error bars show
1001 analytical uncertainties on measured concentrations and subsequent uncertainties in model
1002 results.

1003 Figure 8: simulation results for the CS1 spring over the whole range of the water discharges
1004 from the spring. Results are presented for H_4SiO_4 and Na^+ concentrations (8A and 8C), pH (8D)
1005 and mean water transit time (8B). Red lines indicate simulated parameters after integration
1006 along the flow lines, and blue points show measured values from the field campaigns realized
1007 between 2005 and 2015 (data in table 1 and in supplementary table EA1). Error bars show
1008 analytical uncertainties on measured concentrations and subsequent uncertainties in model
1009 results.

1010 Figure 9: simulation results for the PZ3 and PZ5 piezometers for a strong flood event
1011 (05/05/2015). At the top, active parts of the flow lines that bring the waters to the two sampling
1012 sites are shown (9A and 9B). Below, simulated chemical compositions of the piezometer waters
1013 after integration along the flow lines and comparison with the initial soil solution and the water

chemistry data (9C and 9D). Error bars show analytical uncertainties on measured concentrations and subsequent uncertainties in model results.

Figure 10: simulation results for the CS2 spring. At the top, active parts of the flow lines that bring the waters to the CS2 spring for an important drought (29/11/2011) and a strong flood event (30/03/2010) are shown (10A and 10B). The location of the CS2 spring implies a more scatted distribution of the flow lines than for the CS1 spring. Below, simulation results for the CS2 spring over the whole range of the water discharges from the spring are presented (10C and 10D). Blue lines indicate simulated parameters after integration along the slowest flow line, yellow lines indicate simulated parameters after integration along the fastest flow line, and blue points show measured values from the field campaigns realized between 2005 and 2015 (data in table 1 and in supplementary table EA2). Error bars show analytical uncertainties on measured concentrations and subsequent uncertainties in model results.

Figure 11: simulation results for the RH3 spring chemistry and for a flood event (30/03/2010). On the left, simulated concentrations for the case assuming that the flow lines only run on gneiss (GN) are shown (11A). On the right, simulated concentrations for the case assuming that the flow lines only run on hydrothermally altered granite (VS) are presented (11B). Error bars show analytical uncertainties on measured concentrations and subsequent uncertainties in model results.

Figure 12: overview of the flow lines of the subsurface that feed with water the geochemical sampling sites CS1, PZ3 and PZ5 on May 5th, 2015 according to the NIHM simulations. The

simulated chemical compositions after geochemical integration along the flow lines are also presented for this transect on the southern part of the watershed (CS1, PZ3 and PZ5) and compared with the initial soil solution and the spring chemistry data.

Table 1: measured pH, water discharges and chemical concentrations of H_4SiO_4, Na^+, K^+, Mg^{2+}, and Ca^{2+} in the waters collected from the sampling sites in the Strengbach catchment. The sampling sites include springs (CS1, CS2, RH3) and piezometers (PZ3, PZ5).

Table 2: Initial and calibrated values of the hydrodynamic parameters of the aquifer in the simulation of the Strengbach catchment by NIHM.

Table 3: Comparison between BET surfaces and geometric surfaces for the major primary minerals present in a granitic context. BET surfaces were measured via gas absorption experiments by [1] Berger et al., 1994; [2] Chou and Wollast, 1985; [3] Lundstrom and Ohman, 1990; [4] Amrhein and Suarez, 1992; [5] Acker and Bricker, 1992; and [6] Guidry and Mackenzie, 2003. Geometric surfaces were recalculated from the granulometric ranges of the minerals and by assuming a spherical geometry.

	Na^+ (mmol/L)	K^+ (mmol/L)	Mg^{2+} (mmol/L)	Ca^{2+} (mmol/L)	H_4SiO_4 (mmol/L)	pH	Water Discharge (L/s)
Spring CS1							
16/09/2008	0.071	0.013	0.017	0.044	0.129	6.28	0.954
30/03/2010	0.074	0.014	0.015	0.043	0.120	5.61	1.523
29/03/2011	0.074	0.013	0.015	0.038	0.145	6.23	0.345
04/10/2011	0.080	0.012	0.016	0.042	0.176	6.57	0.122
29/11/2011	0.088	0.015	0.019	0.034	0.177	6.30	0.098
05/05/2015	0.065	0.012	0.012	0.054	0.121	5.33	1.410
Spring CS2							
30/03/2010	0.090	0.020	0.020	0.080	0.122	6.15	6.274
29/03/2011	0.090	0.020	0.020	0.070	0.144	6.18	0.956
02/08/2011	0.090	0.020	0.020	0.060	0.170	6.50	2.171
04/10/2011	0.100	0.020	0.020	0.070	0.177	6.76	0.413
29/11/2011	0.100	0.020	0.020	0.060	0.180	6.22	0.285
05/05/2015	0.077	0.016	0.018	0.074	0.123	6.14	7.500
Spring RH3							
30/03/2010	0.083	0.028	0.032	0.081	0.127	6.28	-
Piezometer PZ3							
05/05/2015	0.074	0.013	0.011	0.053	0.153	6.29	-
Piezometer PZ5							
05/05/2015	0.072	0.013	0.017	0.058	0.132	6.16	-

Table 1

Parameter	Unit	Initial Value	Calibrated value
Depth of substratum	m	4	See figure 2
Saturated hydraulic conductivity (all zones except the low depth zone at the catchment peak (see figure 2))	$m.s^{-1}$	1.10^{-4}	8.10^{-5}
Saturated hydraulic conductivity (catchment peak)	$m.s^{-1}$	1.10^{-4}	1.10^{-4}
porosity (all zones except the low depth zone at the catchment peak)	-	0.1	0.08
Porosity (catchment peak)	-	0.1	0.2
Residual water content (all zones)	-	0.01	0.01
Specific storage (all zones)	m^{-1}	1.10^{-8}	1.10^{-8}
n (Van genuchten coefficient, all zones)	-	2	2
A (Van genuchten coefficient, all zones)	m^{-1}	1	1.5

Table 2

Mineral	**Mineral density** (g/cm^3)	**Granulometric range** (μm)	**Particle radius** (μm)	**Spherical geometric surface** (m^2/g)	**BET surface** (m^2/g)
Quartz[1]	2.62	< 50	1 - 25	1.150 - 0.046	0.310
Albite[2]	2.60	50 - 100	25 - 50	0.046 - 0.023	0.075
K-feldspar[3]	2.56	< 50	1 - 25	1.170 - 0.047	1.420
Anorthite[4]	2.73	20 - 50	10 - 25	0.044 - 0.111	0.500
Biotite[5]	3.09	150 - 400	75 - 200	0.013 - 0.005	0.240
Apatite[6]	3.19	100 - 200	50 - 100	0.018 – 0.009	0.026

Table 3

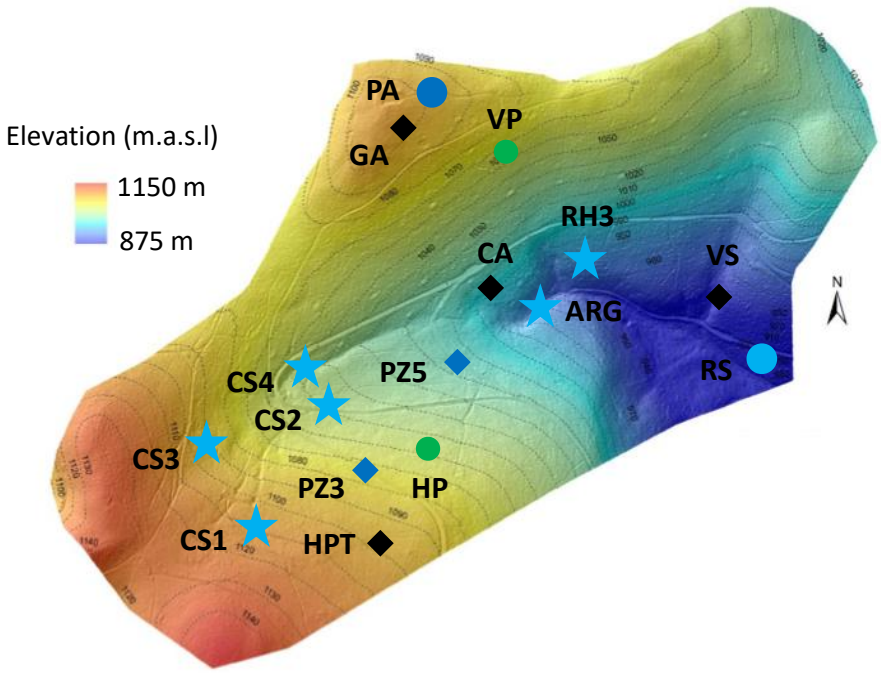
Elevation (m.a.s.l)
1150 m
875 m
PA
VP
GA
RH3
CA
VS
ARG
N
CS4
PZ5
RS
CS2
CS3
PZ3
HP
CS1
HPT

Figure 1

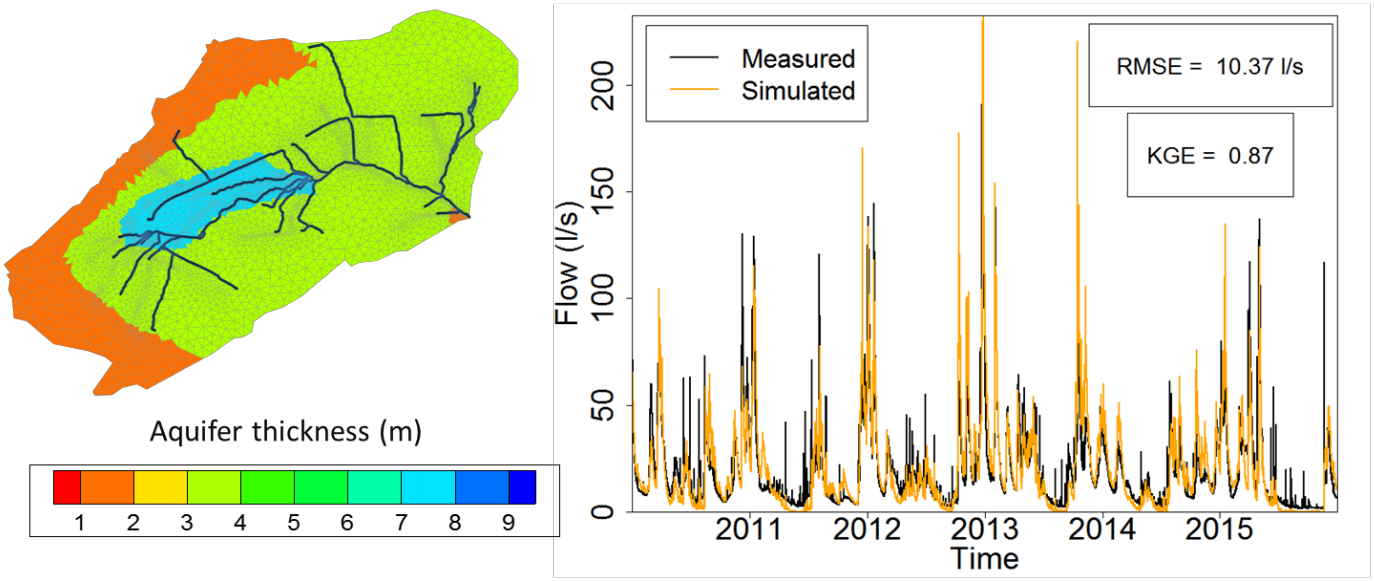
Aquifer thickness (m)
1
2
3
4
5
6
7
8
9
Measured
Simulated
RMSE = 10.37 l/s
KGE = 0.87
Flow (l/s)
0
50
100
150
200
2011
2012
2013
2014
2015
Time

Figure 2

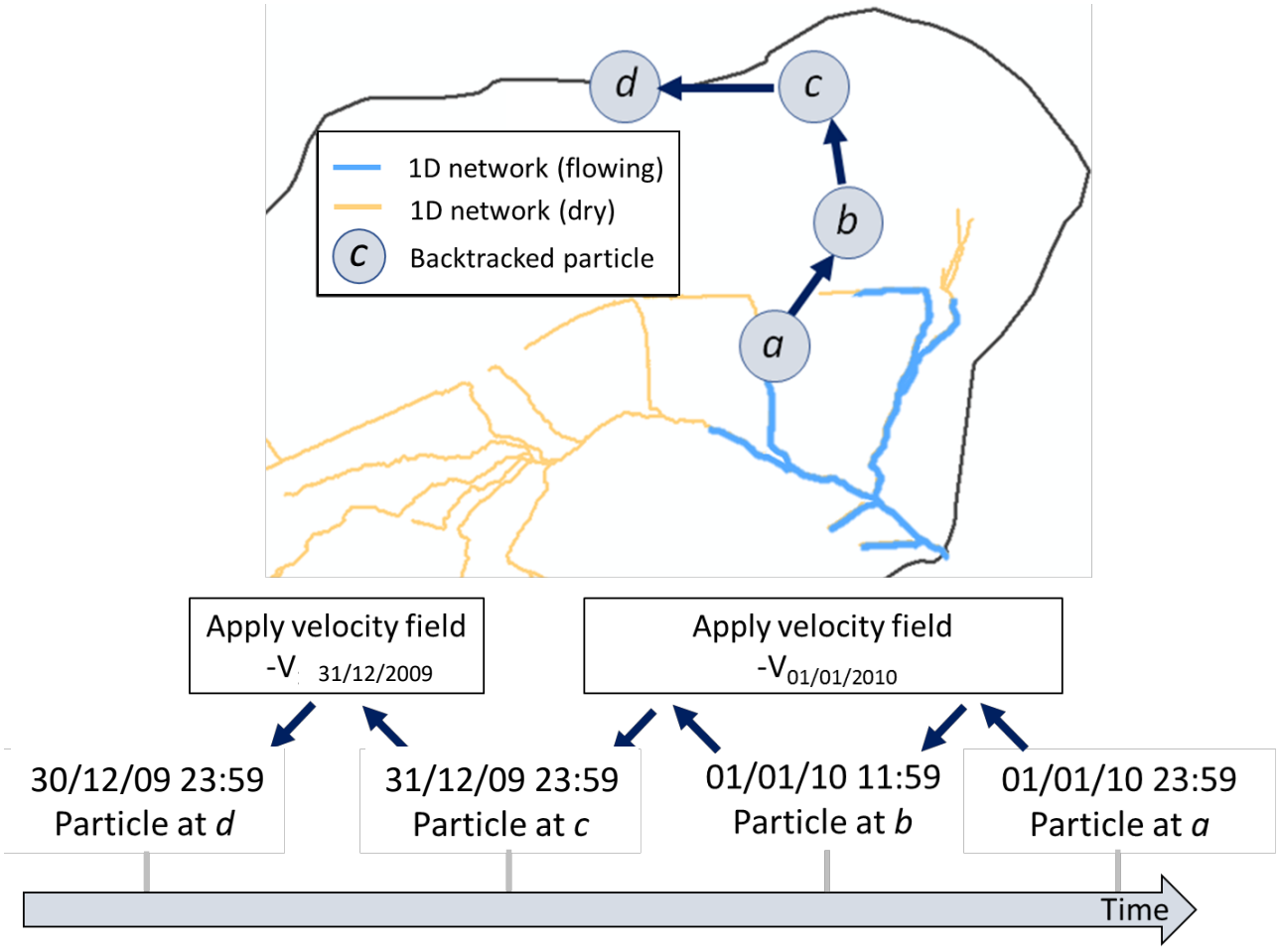
d
c
b
a
1D network (flowing)
1D network (dry)
c
Backtracked particle
Apply velocity field
-V 31/12/2009
Apply velocity field
-V01/01/2010
30/12/09 23:59
Particle at d
31/12/09 23:59
Particle at c
01/01/10 11:59
Particle at b
01/01/10 23:59
Particle at a
Time

Figure 3

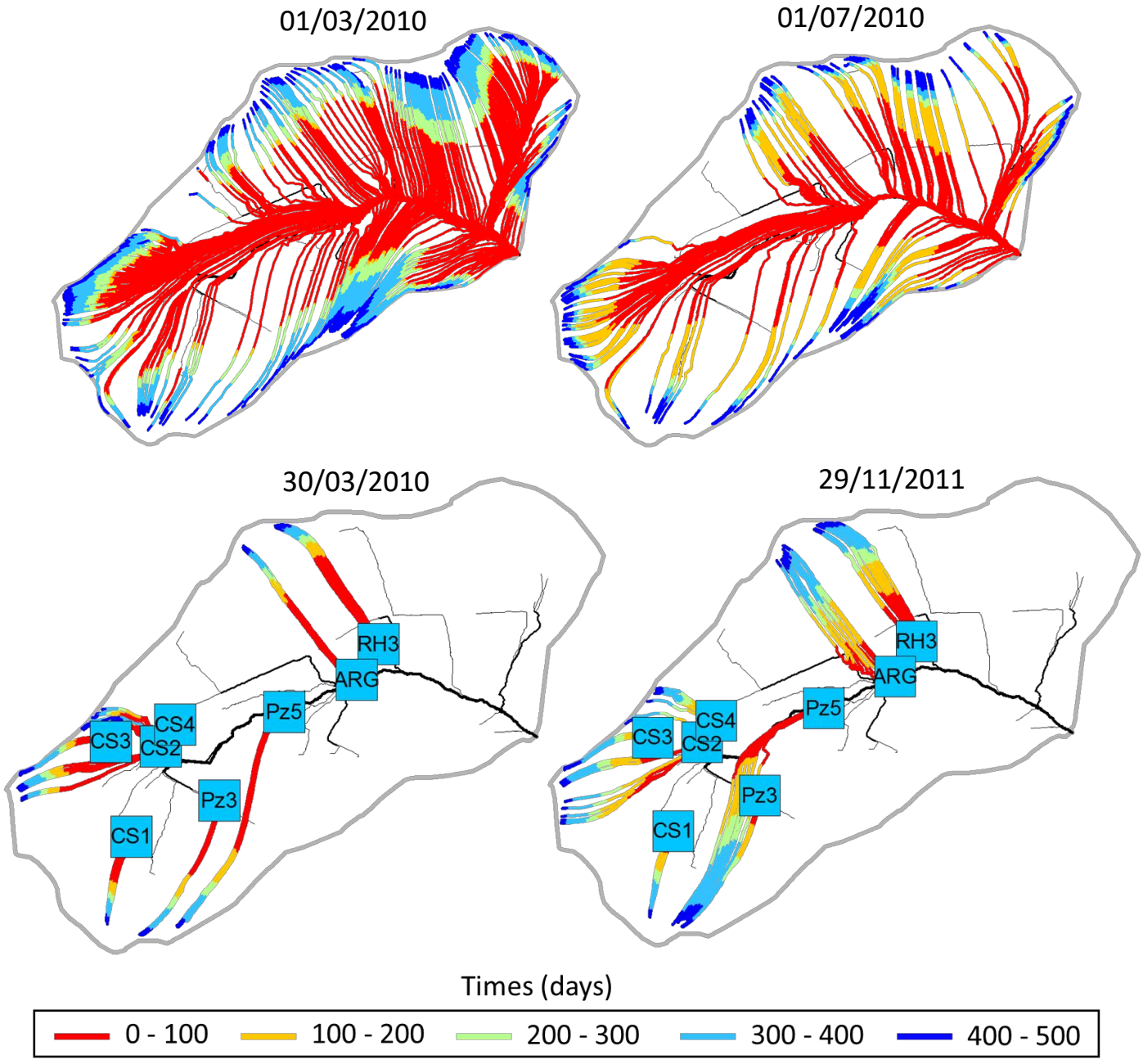
01/03/2010
01/07/2010
30/03/2010
29/11/2011
RH3
ARG
Pz5
CS4
CS3
CS2
Pz3
CS1
Times (days)
0 - 100
100 - 200
200 - 300
300 - 400
400 - 500

Figure 4

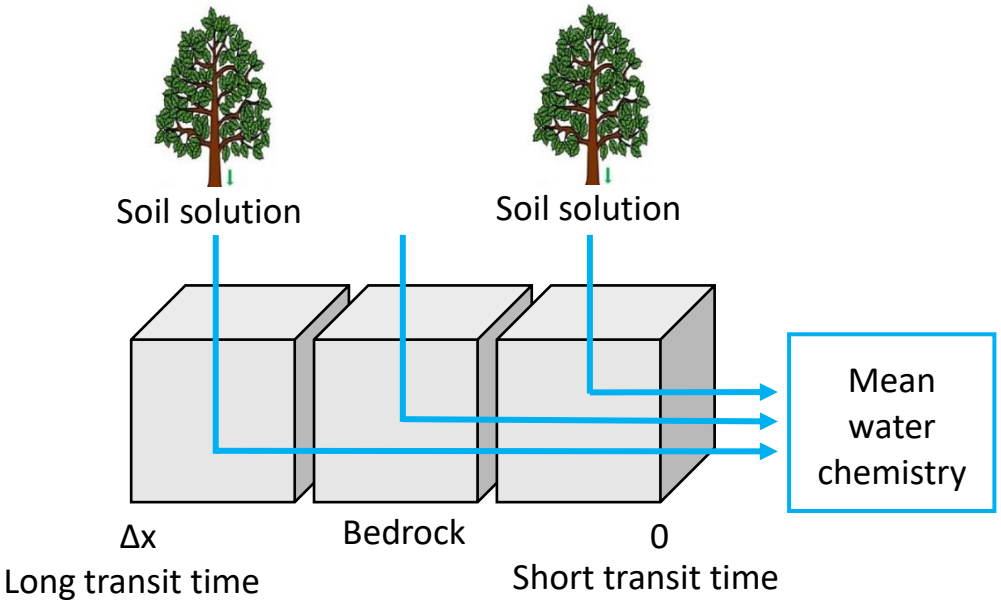
Soil solution
Soil solution
Mean
water
chemistry
Δx
Long transit time
Bedrock
0
Short transit time

Figure 5

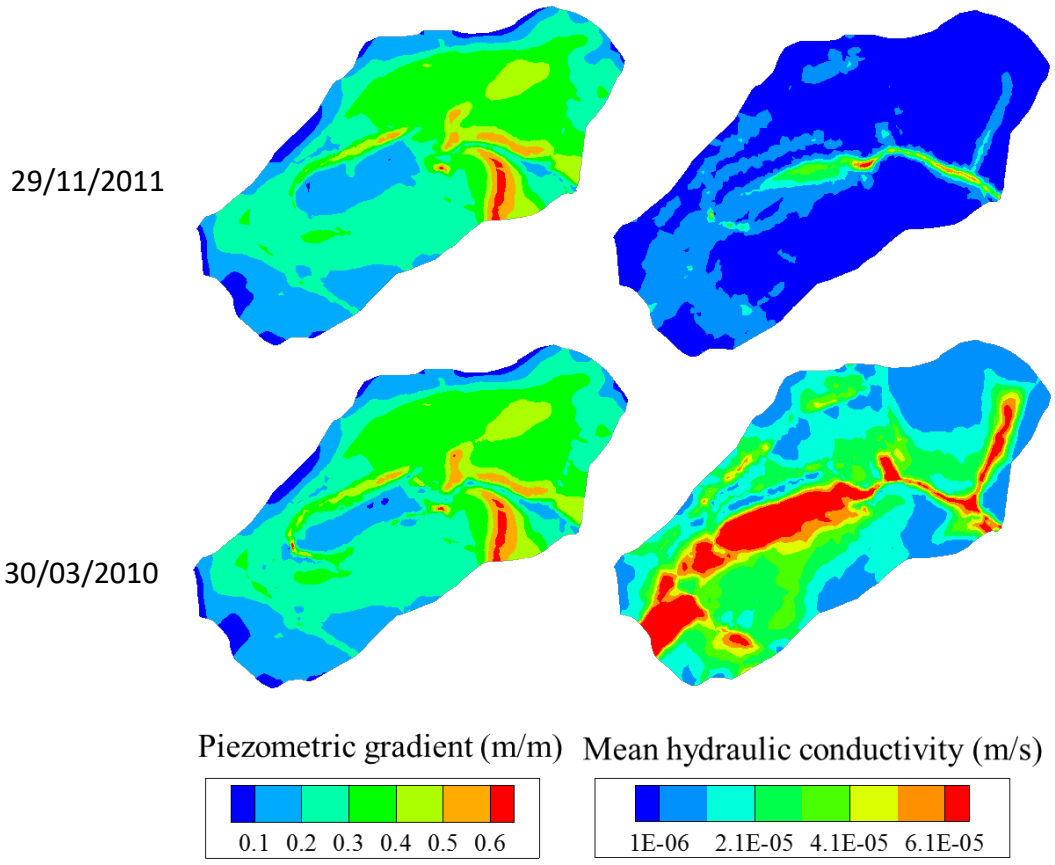
29/11/2011
30/03/2010
Piezometric gradient (m/m)
0.1 0.2 0.3 0.4 0.5 0.6
Mean hydraulic conductivity (m/s)
1E-06 2.1E-05 4.1E-05 6.1E-05

Figure 6

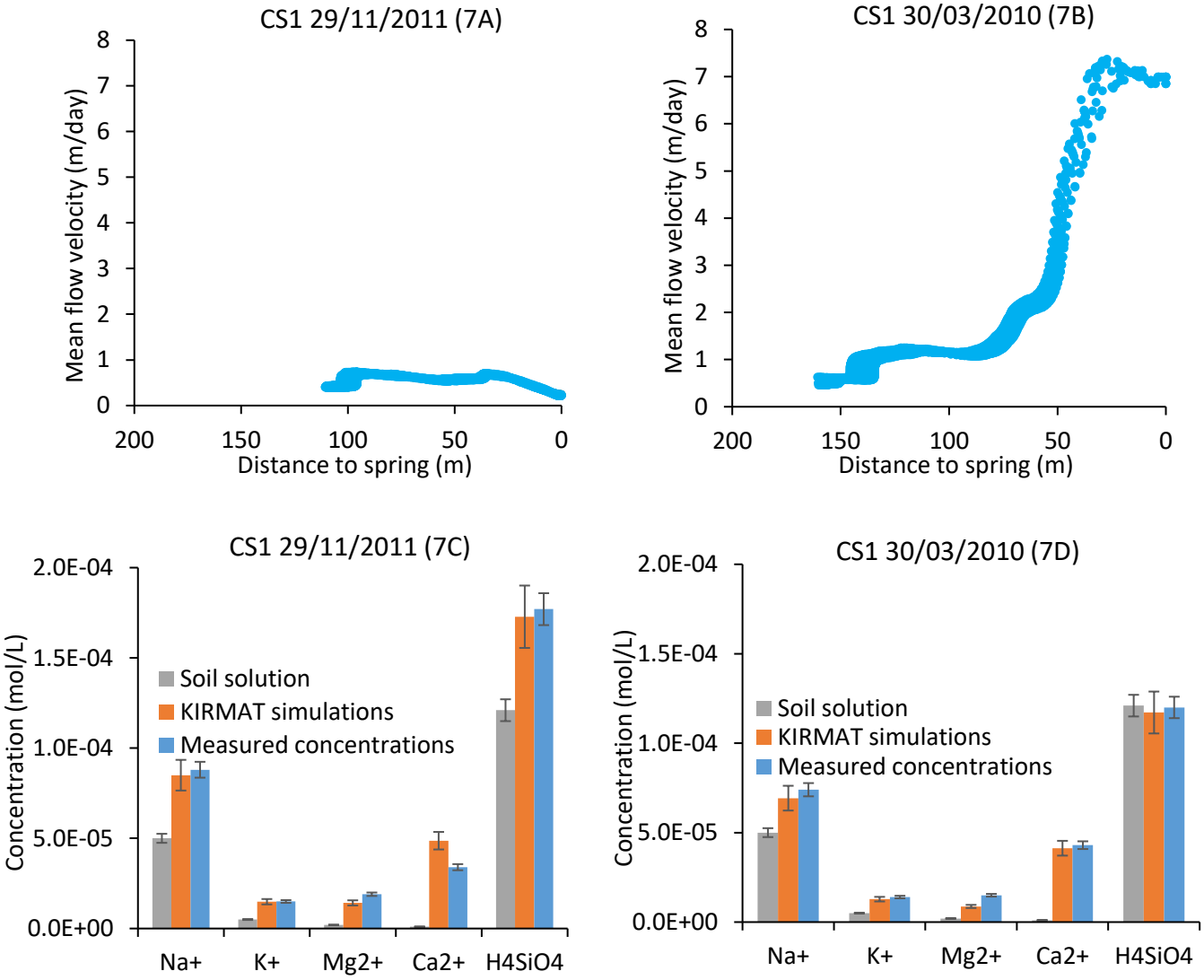
CS1 29/11/2011 (7A)
Mean flow velocity (m/day)
Distance to spring (m)
CS1 30/03/2010 (7B)
Mean flow velocity (m/day)
Distance to spring (m)
CS1 29/11/2011 (7C)
Concentration (mol/L)
Soil solution
KIRMAT simulations
Measured concentrations
Na+
K+
Mg2+
Ca2+
H4SiO4
CS1 30/03/2010 (7D)
Concentration (mol/L)
Soil solution
KIRMAT simulations
Measured concentrations
Na+
K+
Mg2+
Ca2+
H4SiO4

Figure 7

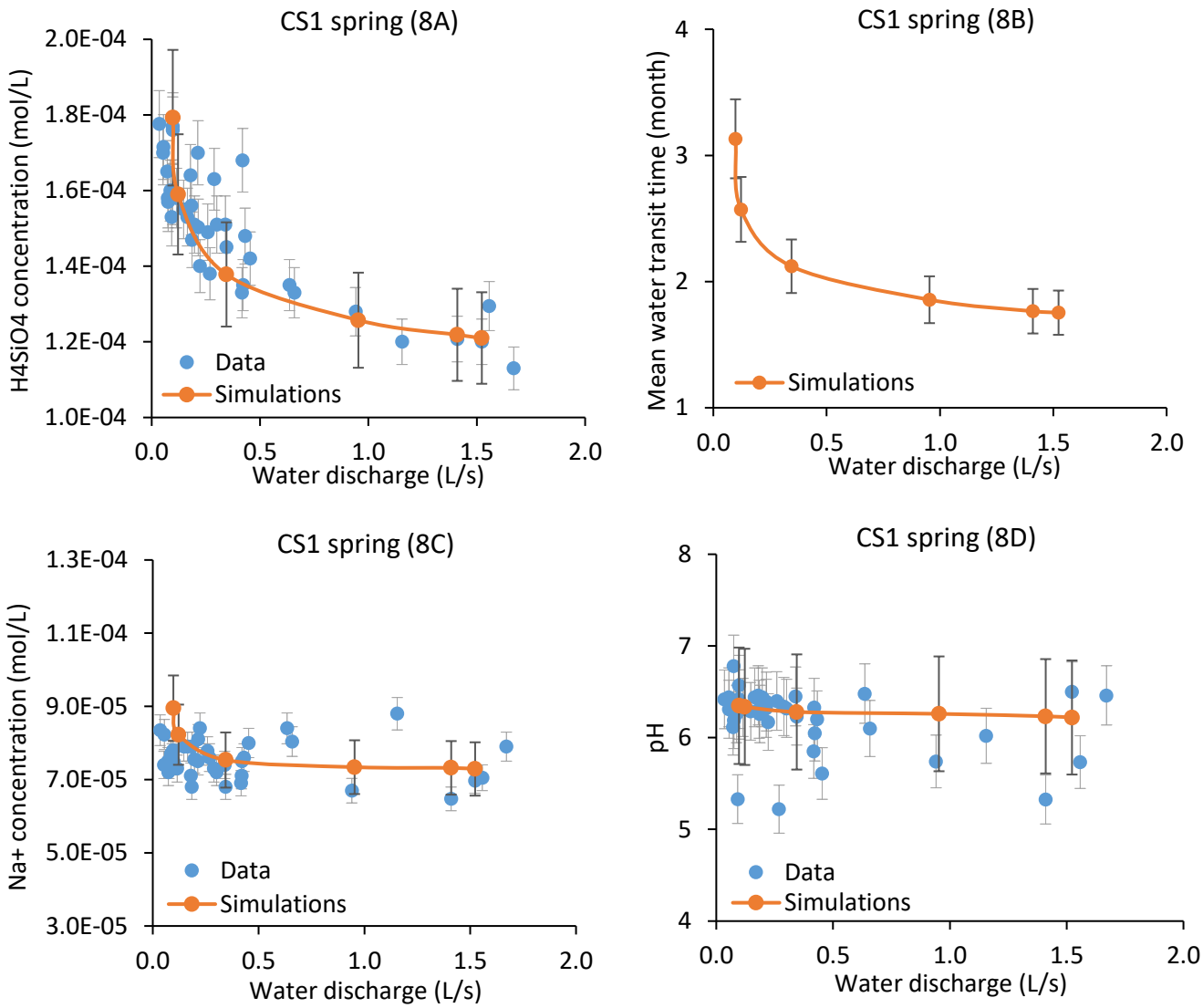
CS1 spring (8A)
H4SiO4 concentration (mol/L)
2.0E-04
1.8E-04
1.6E-04
1.4E-04
1.2E-04
1.0E-04
Data
Simulations
0.0
0.5
1.0
1.5
2.0
Water discharge (L/s)
CS1 spring (8B)
Mean water transit time (month)
4
3
2
1
Simulations
0.0
0.5
1.0
1.5
2.0
Water discharge (L/s)
CS1 spring (8C)
Na+ concentration (mol/L)
1.3E-04
1.1E-04
9.0E-05
7.0E-05
5.0E-05
3.0E-05
Data
Simulations
0.0
0.5
1.0
1.5
2.0
Water discharge (L/s)
CS1 spring (8D)
pH
8
7
6
5
4
Data
Simulations
0.0
0.5
1.0
1.5
2.0
Water discharge (L/s)

Figure 8

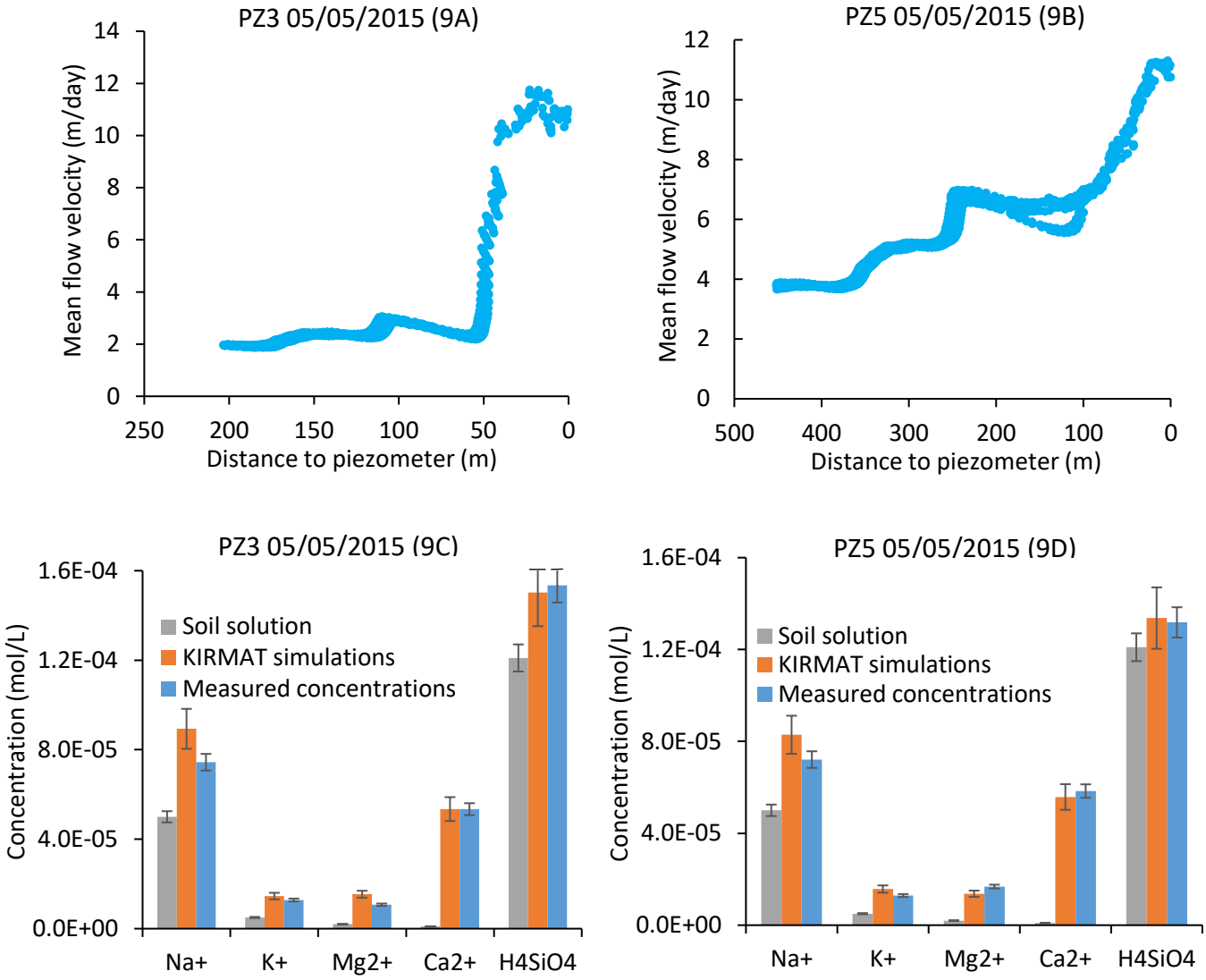
PZ3 05/05/2015 (9A)
Mean flow velocity (m/day)
Distance to piezometer (m)
PZ5 05/05/2015 (9B)
Mean flow velocity (m/day)
Distance to piezometer (m)
PZ3 05/05/2015 (9C)
Concentration (mol/L)
Soil solution
KIRMAT simulations
Measured concentrations
Na+
K+
Mg2+
Ca2+
H4SiO4
PZ5 05/05/2015 (9D)
Concentration (mol/L)
Soil solution
KIRMAT simulations
Measured concentrations
Na+
K+
Mg2+
Ca2+
H4SiO4

Figure 9

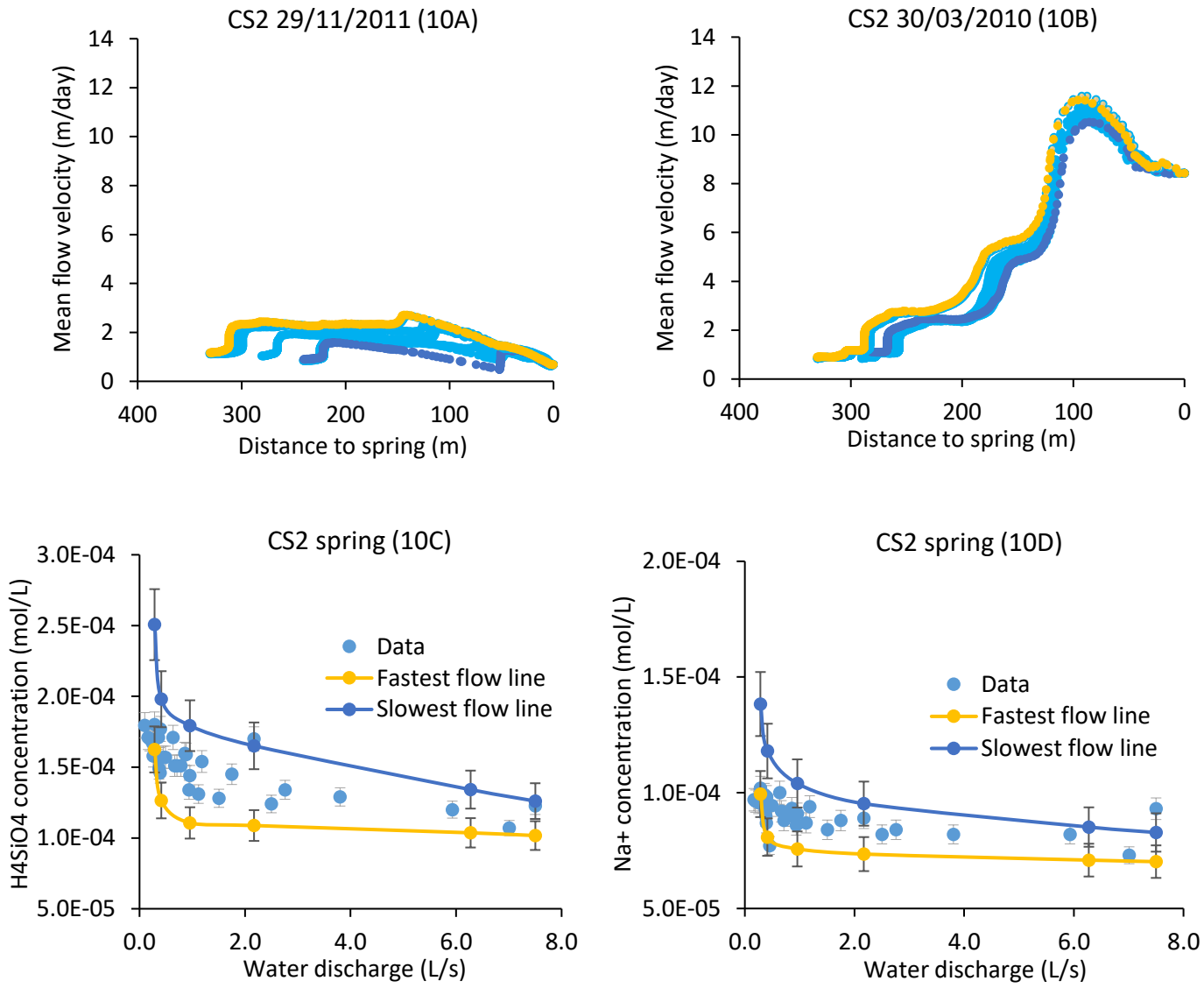
CS2 29/11/2011 (10A)
Mean flow velocity (m/day)
Distance to spring (m)
CS2 30/03/2010 (10B)
Mean flow velocity (m/day)
Distance to spring (m)
CS2 spring (10C)
H4SiO4 concentration (mol/L)
Water discharge (L/s)
Data
Fastest flow line
Slowest flow line
CS2 spring (10D)
Na+ concentration (mol/L)
Water discharge (L/s)
Data
Fastest flow line
Slowest flow line

Figure 10

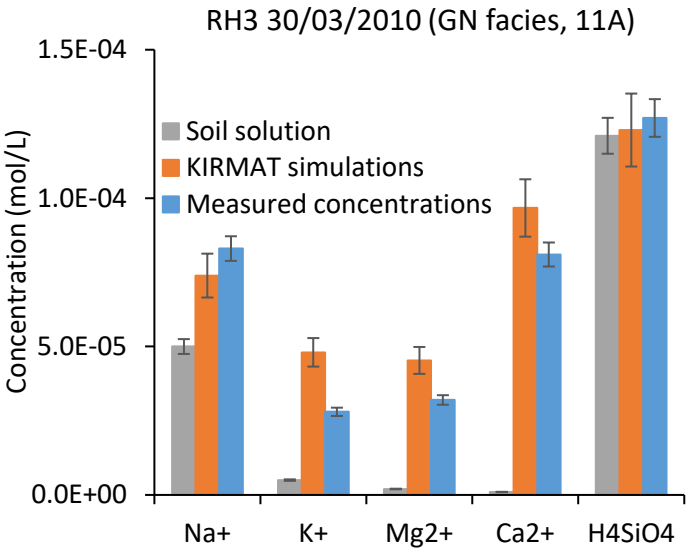
RH3 30/03/2010 (GN facies, 11A)
1.5E-04
1.0E-04
5.0E-05
0.0E+00
Concentration (mol/L)
Soil solution
KIRMAT simulations
Measured concentrations
Na+
K+
Mg2+
Ca2+
H4SiO4

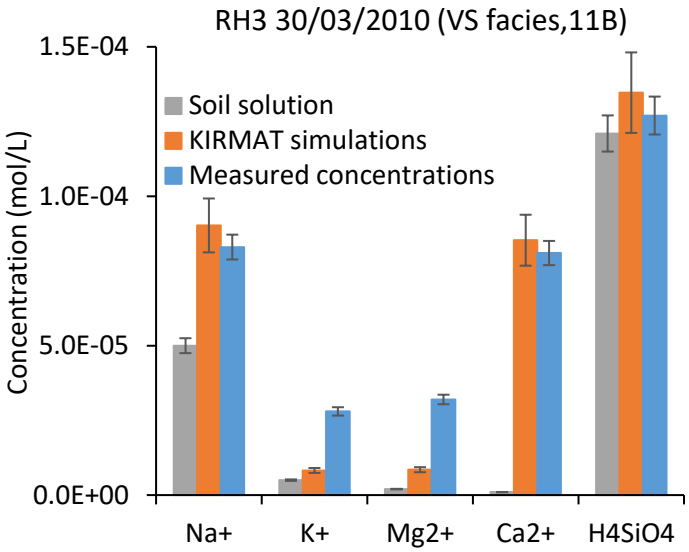
RH3 30/03/2010 (VS facies,11B)
1.5E-04
1.0E-04
5.0E-05
0.0E+00
Concentration (mol/L)
Soil solution
KIRMAT simulations
Measured concentrations
Na+
K+
Mg2+
Ca2+
H4SiO4

Figure 11

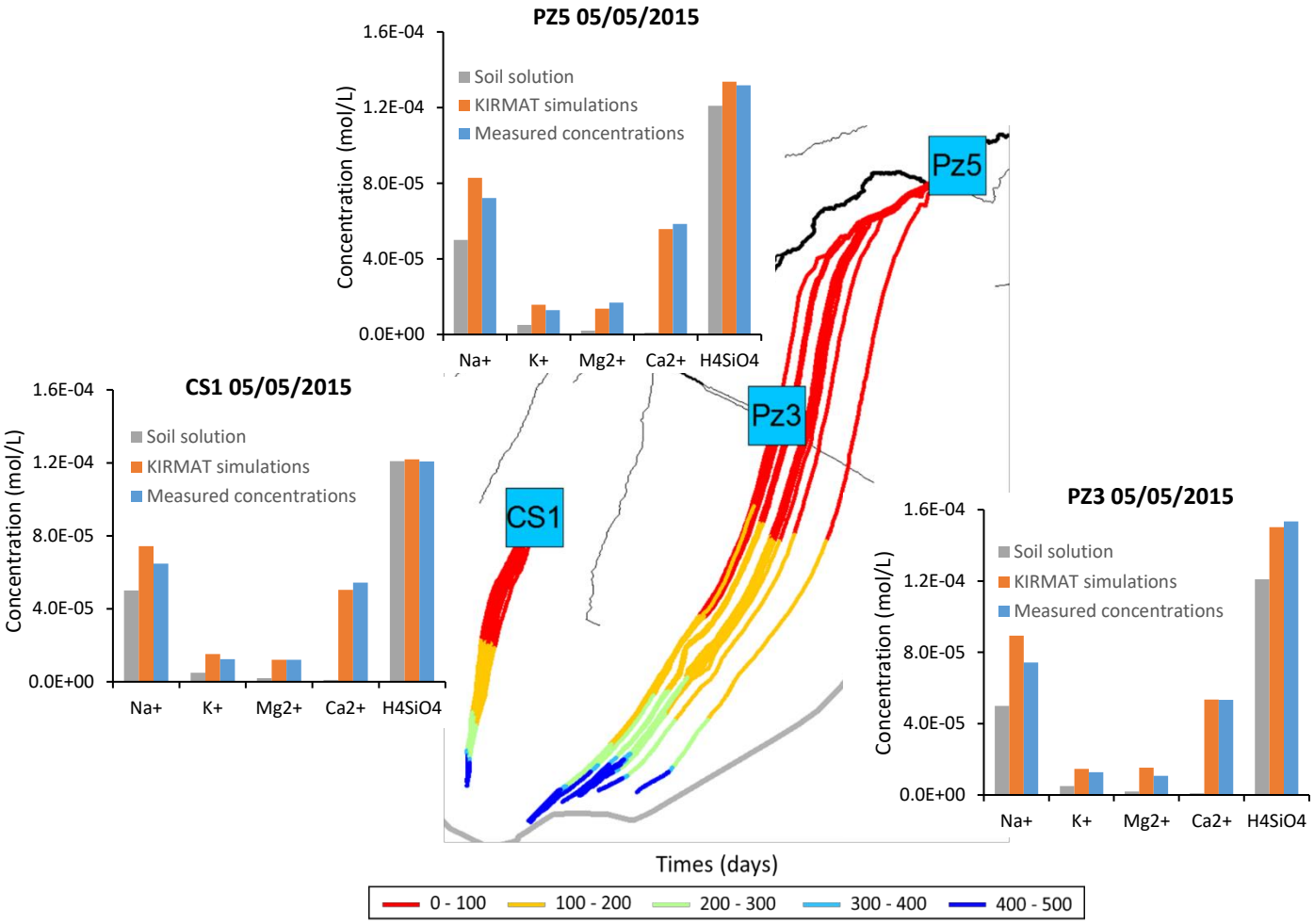
PZ5 05/05/2015
Concentration (mol/L)
1.6E-04
1.2E-04
8.0E-05
4.0E-05
0.0E+00
Soil solution
KIRMAT simulations
Measured concentrations
Na+
K+
Mg2+
Ca2+
H4SiO4
Pz5
Pz3
CS1
CS1 05/05/2015
PZ3 05/05/2015
Times (days)
0 - 100
100 - 200
200 - 300
300 - 400
400 - 500

Figure 12